Solid Earth Discuss., doi:10.5194/se-2017-45, 2017
Manuscript under review for journal Solid Earth
Discussion started: 11 May 2017
© Author(s) 2017. CC-BY 3.0 License.

Solid Earth Discussions
Open Access
EGU

Constraints on the rheology of lower crust in a strike-slip plate boundary: Evidence from the San Quintin xenoliths, Baja California, Mexico

Thomas van der Werf[1], Vasileios Chatzaras[1,2], Leo M. Kriegsman[1,3], Andreas Kronenberg[4], Basil Tikoff[2], Martyn R. Drury[1]

[1] Department of Earth Sciences, Utrecht University, Utrecht, Netherlands
[2] Department of Geoscience, University of Wisconsin-Madison, Madison, Wisconsin, USA
[3] Department of Research & Education, Naturalis Biodiversity Center, Leiden, Netherlands
[4] Department of Geology and Geophysics, Texas A&M University, College Station, Texas, USA

Correspondence to: Vasileios Chatzaras (V.Chatzaras@uu.nl)

Abstract. The rheology of lower crust and its time-dependent behavior in active strike-slip plate boundaries remain poorly understood. To address this issue, we analyzed a suite of mafic granulite and lherzolite xenoliths from the Holocene San Quintin volcanic field, of northern Baja California, Mexico. The San Quintin volcanic field is located 20 km east of the Baja California shear zone, which accommodates the relative movement between the Pacific plate and Baja California microplate. Combining microstructural observations, geothermometry and phase equilibria modeling we constrain that crystal-plastic deformation took place at temperatures of 750–900 °C and pressures of 400–580 MPa, corresponding to 15–22 km depth. A hot crustal geothermal gradient of 40 °C/km is required to explain the estimated deformation conditions. Infrared spectroscopy shows that plagioclase in the mafic granulites is dry. Microstructural evidence suggests that the mafic granulite and peridotite xenoliths were dominantly deforming by processes transitional between dislocation creep and diffusion creep. Recrystallized grain size paleopiezometry yields similar differential stresses in both the uppermost lower crust and upper mantle. Using dry-plagioclase and dry-olivine flow laws we demonstrate that the viscosity of the lower crust and upper mantle is low ($2.2 \times 10^{18} - 1.4 \times 10^{20}$ Pa s). Comparing the viscosity structure of the lithosphere constrained from the San Quintin xenoliths with results from post-seismic relaxation studies from western US, we suggest that lower crust is stronger during transient deformation (e.g., post-seismic relaxation period) while the upper mantle is stronger during long-term deformation (e.g., interseismic period).

1 Introduction

The rheology of lower crust in plate boundary zones is poorly constrained. Experimentally derived flow laws suggest relatively low long-term strength for the lower crust, particularly with respect to middle crust and uppermost mantle, when the latter is dry (e.g., Brace and Kohlstedt, 1980; Kohlstedt et al., 1995). In contrast, a relatively strong lower crust is suggested by post-seismic relaxation studies (e.g., Pollitz et al., 2001; Freed and Bürgmann, 2004; Thatcher and Pollitz, 2008) and the presence of earthquakes in the lower crust (e.g., Jackson, 2002; Reyners et al., 2007). The compositional heterogeneity of the lower crust makes generalization of its rheology difficult to assess. Finally, the lower crust shows a time-dependent behavior with a decreasing strength over larger time scales of observation and/or strain localization (e.g., Thatcher and Pollitz, 2008; Gueydan et al., 2014).

High-temperature deformation of plagioclase, the major rock forming mineral in lower crust, has been studied in the laboratory under the two end-member deformation mechanisms of grain-size ~~sensitive~~ dislocation creep and grain size ~~in~~sensitive diffusion creep (Wilks and Carter, 1990; Rybacki and Dresen, 2000; Dimanov and Dresen, 2005). However, deformation of plagioclase by a mechanism transitional between grain-size insensitive and grain size sensitive creep is being recognized more commonly as a key process in naturally deformed plagioclase-bearing rocks (Kenkmann and Dresen, 2002;

Solid Earth Discuss., doi:10.5194/se-2017-45, 2017
Manuscript under review for journal Solid Earth
Discussion started: 11 May 2017
© Author(s) 2017. CC-BY 3.0 License.

Mehl and Hirth, 2008; Svahnberg and Piazolo, 2010; Hansen et al., 2013; Miranda et al., 2016). It is therefore important to understand how the activity of such a transitional deformation mechanism influences the time-dependent rheological behavior of lower crust in actively deforming regions.

In this study, we investigate the rheology of continental lower crust by analyzing microstructures preserved in granulite xenoliths from northern Baja California, Mexico. The xenoliths were entrained in basalts erupted in the Holocene San Quintin volcanic field, which is located ~20 km east of the Baja California Shear zone (Fig. 1). The Baja California shear zone accommodates the relative movement between the Pacific plate and the Baja California microplate (e.g., Dixon et al., 2000; Plattner et al., 2009). Microstructures from the San Quintin lower crustal and upper mantle xenoliths allow us to investigate the active deformation mechanisms and viscosity structure of the lithosphere near an active, strike-slip plate boundary.

2 Geological setting

2.1 Geology of the Baja California microplate

The Baja California microplate comprises a lithospheric fragment within the Pacific-North America plate boundary that broadly coincides with the Baja California peninsula (Fig. 1). The Baja California microplate formed by tectonic interaction of the Pacific, Farallon, and North American plates (e.g., Atwater and Stock, 1998). Transcurrent motion along the western margin of the North American plate started at 29 Ma, when the Pacific-Farallon spreading center arrived at the trench of the eastward subduction of the Farallon plate beneath North America (Atwater, 1989; Stock and Hodges, 1989). At ca. 12 Ma, deformation along the Pacific-North American plate margin was characterized by significant kinematic partitioning with a component of dextral strike-slip motion along the San Benito and Tosco Abreojos fault zones, west of the Baja California peninsula, and extension in the future Gulf of California area (Stock and Hodges, 1989). The gradual migration of the location of the plate boundary from west to east of Baja California peninsula, between 12 and 3.6 Ma, led to the transfer of Baja California from the North American to the Pacific plate (e.g., Stock and Hodges, 1989). Subsequent transfer of the strike-slip motion to the Gulf of California region led to continental separation of the Baja California peninsula from North America at ca. 3.6 Ma (DeMets, 1995).

Geological observations and GPS measurements show that Baja California behaves as a rigid block (Gastil et al., 1975; Umhoefer and Dorsey, 1997; Plattner et al., 2007). The motion direction of the Pacific plate and Baja California relative to North America is similar, but Baja California moves at a rate that is ~10% slower than the Pacific plate (Dixon et al., 2000; Plattner et al., 2007). Thus, Baja California behaves as a separate microplate, which is only partially coupled to the Pacific plate (Dixon et al., 2000; Plattner et al., 2007, 2009). Dixon et al. (2000) suggest that the relative movement between the Pacific plate and the Baja California microplate is accommodated by offshore slip along several active fault zones, collectively named as the Baja California shear zone (BCSZ). The BCSZ includes the San Clemente-San Isidro fault zone along northern Baja California (Legg et al., 1991), and may continue southward to the Tosco-Abreojos (Spencer and Normark, 1979), the Santa Margarita-San Lazaro (Fletcher et al., 2000), and/or the Todos Santos fault zones (Fletcher and Munguía, 2000) (Fig. 1).

The Baja California microplate consists dominantly of the ~800-km-long Peninsular Ranges batholith (Fig. 1). The batholith is subdivided into a western and eastern plutonic zone, which reflect intrusions into crust of oceanic and continental affinity, respectively (Gastil, 1975; Silver and Chappel, 1988). The western zone of the batholith consists of Middle Jurassic (?) to middle Cretaceous plutons ranging in composition from gabbro to tonalite (Silver and Chappel, 1988). The plutonic bodies intrude lower greenschist grade metamorphic rocks of volcanic arc assemblage and are variably overprinted by subsolidus ductile deformation (Gastil, 1975; Todd et al., 1988). The eastern zone is dominated by early Mesozoic to Late Cretaceous plutons of tonalite, granodiorite, and granite composition (Gastil, 1975; Silver and Chappel, 1988). These

Solid Earth Discuss., doi:10.5194/se-2017-45, 2017
Manuscript under review for journal Solid Earth
Discussion started: 11 May 2017
© Author(s) 2017. CC-BY 3.0 License.

plutons intrude Paleozoic sedimentary rocks, which have been metamorphosed to upper greenschist and amphibolite facies conditions (Gastil and Miller, 1993). Regional metamorphism and deformation in the Baja California peninsula took place synchronously with the intrusion of the Peninsular Ranges batholith (Gastil, 1975; Todd et al., 1988). The mafic composition of the western Peninsular Ranges batholith produces magnetic anomalies and seismic velocity contrast, which can be traced down to at least 20 km depth (Langenheim and Jachens, 2003). The crustal thickness increases from 21–26 km along the eastern Baja California peninsula to 29–38 km in the western Peninsular Ranges batholith (Lewis et al., 2001; Paulssen and De Vos, 2016).

Geophysical studies reveal a complex, heterogeneous upper mantle structure underneath the Baja California peninsula and the Gulf of California (Long et al., 2010; Zhang et al., 2012). The presence of a high shear wave velocity anomaly beneath the central and southern Gulf of California has been interpreted as a slab fragment derived from the Farallon plate (Zhang et al., 2012). Low shear-wave velocity beneath northern Baja California peninsula has been attributed to asthenospheric upwelling within a slab window (Zhang et al., 2012; Paulssen and De Vos, 2016). The existence of a slab window beneath the northern part of the peninsula was also inferred from plate reconstructions and volcanism (Atwater, 1989; Dickinson, 1997). In the same region, the fast propagation direction of surface waves in the crust and uppermost mantle are plate-boundary parallel, whereas the fast anisotropic directions of the Rayleigh wave phase velocities are oriented E-W - oblique to the plate boundary - at deeper levels (50-150 km) (Zhang et al., 2009).

2.2 The San Quintin volcanic field

Cessation of the subduction of Farallon-derived microplates at ca. 12 Ma was followed by the eruption of several Miocene–Holocene volcanic fields of basaltic to rhyolitic composition along the Baja California peninsula. The northernmost volcanic field is the Upper Pleistocene–Holocene San Quintin volcanic field (Fig. 1), in which the eruptive activity continued until less than 5,000-6,000 years ago (Gastil, 1975; Rogers et al., 1985; Luhr et al., 1995). The San Quintin volcanic field is unique in Baja California because of the intraplate-type alkali olivine alkali-basalts, carrying upper mantle peridotites and lower crustal granulites (Basu, 1975; Rogers et al., 1985; Storey et al., 1989; Luhr et al., 1995). The geochemical signature of the San Quintin intraplate-type basalts points to an asthenospheric source, potentially related to the formation of a slab window beneath northern Baja California as a result of Pacific-Farallon ridge subduction (Storey et al., 1989).

The most important sources of xenoliths in the San Quintin volcanic field are the two northernmost volcanic complexes of Media Luna and Woodford, which are the most differentiated in terms of composition (Basu, 1975; Luhr et al., 1995). The upper mantle xenoliths are highly deformed (Basu, 1977; Cabanes and Mercier, 1988) and provide evidence for a low-viscosity upper mantle (Palasse et al., 2012). Two groups of strained peridotites have been recognized: 1) coarse-grained with equilibrium conditions of T = 1000–1050 °C and P < 2000 MPa; and 2) porphyroclastic and mosaic with equilibrium conditions of T = 800–950 °C and P ≤ 1000 MPa (Basu, 1977; Cabanes and Mercier, 1988). Deformation in the shallow upper mantle has been related to active shear zones, which accommodate the relative motion between the Baja California microplate and the Pacific plate (Cabanes and Mercier, 1988; Palasse et al., 2012). In contrast to the upper mantle xenoliths, we only have very poor constraints for the deformation processes and extraction depths of the lower crustal xenoliths.

3. Methods

3.1 Sample collection and description

We collected crustal and upper mantle xenoliths from the Media Luna (samples starting with the code SQL) and Woodward (SQW) volcanic complexes, which are 3 km apart, and comprise the two northern volcanic complexes of the San Quintin volcanic field (Fig. 1b; Luhr et al., 1995). The maximum length of the sampled xenoliths ranges between 5 and 25 cm. This

Solid Earth Discuss., doi:10.5194/se-2017-45, 2017
Manuscript under review for journal Solid Earth
Discussion started: 11 May 2017
© Author(s) 2017. CC-BY 3.0 License.

study mainly focuses on the mechanical properties and petrology of the crustal xenoliths. Crustal xenoliths are scarce compared to the upper mantle xenoliths in both volcanic complexes; a total of twenty-two crustal xenoliths were sampled (8 from Media Luna and 14 from Woodward). They are subdivided in gabbros (8 samples) and granulites (14 samples). Based on our small sample collection, gabbroic xenoliths are more common in the Media Luna volcanic complex (5 out of 8 sampled crustal xenoliths), while granulite xenoliths are more common in the Woodward volcanic complex (11 out of 14 sampled crustal xenoliths). We studied one lherzolite xenolith, the microstructure, crystallographic texture and seismic anisotropy of which have previously been studied by Palasse et al. (2012). We build on the work of Palasse et al. (2012), by evaluating the mechanical properties of the upper mantle xenolith. Where possible, we visually determined the foliation and lineation in each crustal xenolith using the alignment and elongation of pyroxene grains ~~if possible~~, as well as the banding between plagioclase- and pyroxene-rich layers. Where a mineral shape fabric was identified, we constructed thin sections oriented parallel to the lineation and perpendicular to the foliation. We also investigated one lherzolite xenolith – whose microstructure, crystallographic texture and seismic anisotropy were previously documented by Palasse et al. (2012) – in order to evaluate the mechanical properties of the upper mantle.

3.2 Analysis of mineral chemistry, geothermometry, and phase equilibria

Mineral major and minor element compositions were determined by wavelength-dispersion spectrometry with a JEOL JXA-8530F Hyperprobe field emission electron probe microanalyser in the Electron Microscopy facility at Utrecht University. Operating conditions were 15 kV accelerating voltage, 20 nA beam current, and beam diameter of 1 µm. Compositions were determined for cores and rims in each phase, and where possible, adjacent grains were analyzed. Equilibration temperatures were determined by application of two different calibrations of the two-pyroxene geothermometer, namely, those by Brey and Köhler (1990) (BK90), and Taylor (1998) (T98). Temperatures were calculated at a pressure of 600 MPa. The effect of pressure on calculated two-pyroxene temperatures is only 0.02 °C/MPa. Phase equilibria for four crustal xenoliths were computed using Perple_X (Connolly and Petrini, 2002 version 07). The updated internally consistent thermodynamic dataset of Holland and Powell (1998; 2002 updated version) was used to construct the P-T pseudosections, and the relevant solution models come from the PERPLE_X solution model files.

3.3 Water content analysis

To determine the H_2O contents of plagioclase grains, we measured the infrared spectra of individual plagioclase grains using a JASCO-IRT-30 infrared microscope that is attached to a JASCO FT/IR-470 plus FTIR spectrometer housed at the Experimental Rock Deformation/HPT lab, in the Department of Earth Sciences, at Utrecht University. The microscope is equipped with a Mercury Cadmium Tellurium (MCT) detector cooled by liquid nitrogen. The sample stage is built into a chamber that is constantly supplied by nitrogen gas during the measurements to reduce the influence of CO_2 gas and H_2O vapor. Grains of the samples were not oriented and the IR light was unpolarised. An aperture of 100 x 100 µm was used to select areas free of cracks, optical-scale inclusions and boundaries under the microscope. Infrared spectra were first taken without the samples to remove the radiation background from sample measurements. The spectra were measured at room temperature, compiling 150 scans for each spectrum collected between wavenumbers of 1 cm^{-1} to 4000 cm^{-1} with a resolution of 4 cm^{-1} at room temperature. Spectra were collected from at least five grains in each sample. Absorbances were determined quantitatively (recording peak height above background and integrated area below the peaks) using the JASCO software. Most spectra had sloping backgrounds due to scattering, which were adjusted using the JASCO software. The H_2O content in plagioclase was determined using the Beer-Lambert law constrained by the calibration of Johnson and Rossman (2003). Because the orientation of the grains is unknown, we compared our measurements of integrated absorbances of OH bands in unpolarized IR spectra with the integrated absorbances in the three principal vibration directions of anorthite, digitizing polarized spectra of Johnson and Rossman (2003; their Fig. 1a). Using the ratios between these

Solid Earth Discuss., doi:10.5194/se-2017-45, 2017
Manuscript under review for journal Solid Earth
Discussion started: 11 May 2017
© Author(s) 2017. CC-BY 3.0 License.

values and the total integrated absorbance, we determined the minimum and maximum values for the integrated absorbance for three principal vibrational directions to obtain upper and lower bounds for H_2O content, based on our unpolarized spectra, rather than reporting a single number (Table S1). This approach gives a range of OH contents for unpolarized IR, within which the OH content is estimated conservatively, given that radiation with vibrational directions other than the principal maximum and minimum absorbances are also included in unpolarized IR measurements. Somewhat lower bounds for water content are given when we use the same procedure for the more recent calibration of Mosenfelder et al. (2015).

3.4 Analysis of crystallographic preferred orientations

Thin sections were mapped using scanning electron microscopy (SEM) in combination with electron backscatter diffraction (EBSD). Automated EBSD data acquisition was performed using a FEI XL30S field emission SEM equipped with an Oxford Instruments NordlysNano EBSD detector at the EM square facility at Utrecht University. Large area (~200 mm^2) crystallographic orientation maps were acquired using the Oxford Instruments AZtecHKL acquisition and analysis software (version 3.0). A step size of 10 µm was used. Post-acquisition data treatment involved processing of EBSD maps using the HKL Channel5 software package. Processing included: 1) removal of isolated single pixels differing by more than 10° from their neighbors; and 2) assignment of the average orientation of neighboring pixels to non-indexed pixels with eight nearest neighbors. This operation was iterated until no new pixels were filled and was repeated for non-indexed pixels with decreasing number of nearest neighbors as low as five. To quantify the strength of olivine crystallographic preferred orientation (CPO) we used the J-index (Bunge, 1982).

3.5 Grain size analysis and paleopiezometry

To determine the mean recrystallized grain size of plagioclase, clinopyroxene, and olivine we used the equivalent circular diameter method on grains defined by a grain boundary misorientation angle of 10°, constructed from the EBSD data in HKL Channel5 software. We used the open-source GrainSizeTools script (Lopez-Sanchez and Llana-Fúnez, 2015) to construct grain size distributions of the number-weighted equivalent circular diameters. We determined the arithmetic mean of the grain size distributions. To convert between the mean equivalent circular diameter on a two-dimensional section and the mean grain size in three dimensions, a scaling factor of 1.2 was used (Underwood, 1970).

For viscously deforming rocks, the paleopiezometric relationship that relates the recrystallized grain size to the differential stress has the form:

$$\sigma = Bd^{-n} \quad (1)$$

where σ is the differential stress, d is the recrystallized grain size, and B and n are empirically derived constants. To estimate differential stress, we used the theoretical paleopiezometer of Twiss (1977) for plagioclase, the calibration of Avé Lallement (1978) for clinopyroxene, and the calibration of Van der Wal et al. (1993) for olivine. In one olivine-bearing granulite, we estimated the olivine mean subgrain size using the linear intercept method on an EBSD map (Valcke et al., 2006). To define the lower limit of subgrain and grain boundaries we used a misorientation angle of 1° and 10°, respectively. To convert between mean intercept length on a two-dimensional section and the mean grain diameter in three dimensions, a scaling factor of 1.5 was used (Underwood, 1970). We used the subgrain-size paleopiezometer of Toriumi (1979) to estimate the range of differential stresses for olivine.

4 Results

4.1 Microstructures

Microstructures in the San Quintin xenoliths were studied by combined optical (Fig. 2) and electron microscopy (e.g., SED-BSE and EBSD maps; Fig. 3) techniques. The gabbroic xenoliths have a cumulate microstructure, characterized by the

Solid Earth Discuss., doi:10.5194/se-2017-45, 2017
Manuscript under review for journal Solid Earth
Discussion started: 11 May 2017
© Author(s) 2017. CC-BY 3.0 License.

crystallization of earlier pyroxenes and interstitial growth of optically continuous pools of plagioclase (Fig. 2a). Plagioclase grains in gabbros are centimeter sized and contain growth twins. The rare presence of tapered deformation twins and the lack of undulatory extinction indicate that plagioclase in the gabbroic xenoliths is only weakly deformed by plastic mechanisms.

Granulites have a compositional foliation defined by alternating plagioclase- and pyroxene-rich domains (Fig. 3a). The pyroxene-rich domains form elongated lenses, aligned parallel to the foliation (Figs. 2b and 3a). The granulite xenoliths have a granoblastic microstructure; plagioclase and pyroxenes are characterized by gently curved to straight grain and/or phase boundaries, which lead to polygonal grain shapes with approximately 120° triple junctions (Fig. 3c). Grain and phase boundaries of plagioclase and pyroxene are either concave or straight and aligned (Figs. 2c and 3c, d). Straight and aligned grain boundaries are associated with the formation of quadruple junctions (Figs. 2e and 3c, d). Large plagioclase grains (porphyroclasts) contain deformation twins, and show undulose extinction, and the formation of subgrain boundaries concentrated along grain boundaries (Fig. 3b). Smaller, recrystallized plagioclase grains are usually devoid of mechanical twins; where present, the twins trend parallel to the mechanical twins of neighboring plagioclase porphyroclasts.

Clinopyroxene grains exhibit core-and-mantle structures (Fig. 2b); the clinopyroxene porphyroclasts show undulose extinction and subgrains, and are surrounded by smaller recrystallized clinopyroxene grains. Formation of subgrain boundaries in the clinopyroxene porphyroclasts is concentrated along grain boundaries. Clinopyroxene porphyroclasts show thin orthopyroxene exsolution lamellae (e.g. SQW-75; Fig. 2b), which are attributed to cooling.

Olivine in the crustal xenoliths is either present in symplectites with intergrown pyroxenes, plagioclase, and spinel (Fig. 4a, b), or forms rims around pyroxene grains. In both types of microstructure, olivine is fine grained and shows no evidence of intracrystalline deformation. The two-pyroxene granulite SQ-16 is the only xenolith containing lenses of cumulate olivine (Fig. 3a). This type of olivine is coarse grained, shows undulose extinction, and exhibits development of subgrain boundaries oriented perpendicular or oblique (at high angle) to the foliation. Straight to concave olivine-olivine grain boundaries, leading to polygonal crystal shapes with 120° triple junctions, are indicative of an equilibrium microstructure. This olivine type is rimmed by a thick orthopyroxene corona, which may result from the interaction between olivine and basaltic melt. Importantly, this is also the Mg-richest olivine and the only one lacking Fe^{3+} and Mn (Table S3). In some xenoliths (e.g., SQW-115; Fig. 4c), orthopyroxene grains have large olivine rims, which is opposite to the orthopyroxene coronas on xenocrystic olivine in SQ-16. In SQW-115, EDS and WDS analyses revealed the presence of clinopyroxene and plagioclase in the coronas, in addition to olivine.

Further information about late processes that involve melt-rock interaction and late oxidation are provided by the following microstructural observations: 1) symplectites in SQW-75 (Fig. 4a) show intergrowths of spinel, orthopyroxene, plagioclase and olivine, that appear to be derived from the breakdown of an earlier generation of clinopyroxene; some involvement of a high-T anhydrous basaltic melt is likely, as it facilitates the reaction balance; 2) crystallized melt patches in some xenoliths (e.g., SQ-16) are unaffected by deformation (Fig. 2d); and 3) magnetite coronas resulting from late oxidation are present around spinel grains (Fig. 4d).

The lherzolite xenolith examined in this study (SQ2-68) has an equigranular mosaic microstructure; it contains elongated (aspect ratio of 11:1) pyroxene porphyroclasts within a fine-grained matrix of equant olivine and pyroxene grains (Palasse et al., 2012). Complementing the microstructural observations of Palasse et al. (2012), we report the existence of straight grain boundaries and quadruple junctions (Fig. 2f).

4.2 Mineral content and chemistry

The lower crustal xenoliths have a mafic composition, and dominantly consist of plagioclase and clinopyroxene, with lesser amounts of orthopyroxene, olivine and spinel. A few samples contain subordinate magnetite and ulvöspinel. A felsic granulite (SQW-76) sampled from the Woodward volcanic complex consists of plagioclase + quartz + orthopyroxene +

Solid Earth Discuss., doi:10.5194/se-2017-45, 2017
Manuscript under review for journal Solid Earth
Discussion started: 11 May 2017
© Author(s) 2017. CC-BY 3.0 License.

magnetite + titanite. Table S2 shows the mineral content of each xenolith used for phase equilibria modeling (see section 4.3). All mineral phases show multiple generations, with compositions commonly dependent on the microstructure. Most phases are chemically unzoned, except plagioclase. Table S3 shows representative mineral compositions determined with electron probe microanalysis.

Plagioclase is present in two general variations in all examined samples: as relative large grains that form a major part of the xenoliths and as small grains in the symplectites and exsolution textures. The large grains are unzoned and An-rich (> An80) (Fig. 5). The smaller grains locally show compositional zoning and have much lower anorthite content (An40−60). The lowest An content (An65, andesine) was measured in enderbitic sample SQW-76. The orthoclase component is negligible in all samples.

Clinopyroxene shows no evidence for compositional zoning, except in sample SQW-115. Its composition does, however, vary somewhat between samples. In addition, in symplectites (SQW-114) and rims (SQW-115), clinopyroxene has a lower CaO and a higher MgO content compared to the larger grains in the samples.

Orthopyroxene also lacks chemical zoning. Its composition depends on microstructure and assemblage. In symplectites and exsolution structures, the FeO content is lower and MgO content higher than in primary grains. In addition, orthopyroxene has a higher CaO content in symplectites. The Al-content is quite low.

Spinel forms part of a secondary texture (symplectite, exsolution or altered rim). They are Al-rich and have a large amount of ferric iron. The only exceptions are some spinels found in clinopyroxene exsolution in sample SQW-75, which are relatively Cr-rich.

Olivine also generally forms part of a secondary texture and has X_{Mg} ranging from 0.65 to 0.80. The iron content is higher in the olivine of sample SQW-110 (X_{Mg} = 0.39). Large olivine crystals in SQ-16 comprise a primary texture (Fig. 3A); these olivine xenocrysts are rimmed by orthopyroxene and have the highest X_{Mg} value (0.84).

4.3 P-T conditions

P-T pseudosections were reconstructed for three xenoliths: SQ-16, SQW-75, and SQW-114, using the Perple_X software, version 7.0. The pseudosections are based on microprobe data and estimates of volume percentages for specific micro-domains. The determined volume percentages and magnesium numbers for each phase in a domain are shown in Table S2.

Figure 6 shows the constructed P-T pseudosections. The stable mineral assemblages used for constructing the pseudosections are indicated with a red outline. The composition used for SQ-16 is stable between 630 and 700 °C (Fig. 6a). The volume percentages of the phases generally overlap on the boundary between the Plg + Ol + Cpx + Opx + Sp and Plg + Ol + Cpx + Sp stability fields. This indicates that the pressure at that stage is between 300 and 370 MPa. The composition for SQ-16 was based on a symplectite microdomain and thus gives an indication of P-T conditions postdating the peak. It lacks orthopyroxene, which is present in the general mineral assemblage of the sample. Hence, the peak pressure was probably higher for this sample. In addition, the sample shows evidence for cooling from higher T, resulting in thick coronas of orthopyroxene on xenocrystic olivine. In support of this interpretation are the higher equilibrium temperatures (751 ± 27 °C) estimated from two-pyroxene geothermometry (Table 1).

For SQW-75 the pseudosection was based on the whole rock mineral assemblage (Fig. 6b). This assemblage is stable between 680 and 860 °C at 400–530 MPa. Olivine is a secondary phase in this sample and is only present in symplectites and exsolutions. Hence, similar to SQ-16, a stage of decompression has affected the sample.

The pseudosection for SQW-114 was constructed using volume estimates of a melt pocket. Isopleths for Al_2O_3 and X_{Mg} of orthopyroxene give a wide P-T range of 700–980 °C and 450–580 MPa (Fig. 6c).

Temperatures in six xenoliths were estimated using two-pyroxene geothermometry (Table S4). The average temperature estimates range from 750 to 890 °C (Table 1) and fall in two groups: 750–760 °C and 855–890 °C. Except SQ-

Solid Earth Discuss., doi:10.5194/se-2017-45, 2017
Manuscript under review for journal Solid Earth
Discussion started: 11 May 2017
© Author(s) 2017. CC-BY 3.0 License.

16, the temperatures estimated from two-pyroxene geothermometry overlap with the range of temperatures constrained for each xenolith from the P-T pseudosections.

4.4 Water content

Water contents of plagioclase grains were measured in three xenoliths; two mafic granulites (SQW-75, and SQW-115) and one felsic granulite (SQW-76). Figure 7 shows representative spectra for three different grains of each sample in the 2800 – 4000 cm^{-1} range. This region includes the stretching vibration wavenumbers of structural OH and the symmetrical and asymmetrical stretching vibrations of H_2O molecules. There is a clear difference in the spectra of sample SQW-76 with broad OH absorption bands at 3250, 3400, and 3600 cm^{-1} (Fig. 7c) and the samples SQW-75, and SQW-115 with little or no evidence of large OH bands (Fig. 7a, b). The 3250 cm^{-1} absorption band of SQW-76 corresponds well with OH bands of a number of plagioclases reported by Johnson and Rossman (2003), while the large OH bands at 3400 and 3600 cm^{-1} were absent from spectra of their plagioclase specimens. These bands resemble OH bands in other feldspars, and they may even reflect spectroscopic contributions of fluid inclusions (band at 3400 cm^{-1}) and layer silicate inclusions (band at 3600 cm^{-1}). SQW-78 (Fig. 7a) shows bands at 2850 and 2950 cm^{-1} and at 3600 and 3700 cm^{-1}. The bands at 2850 and 2950 cm^{-1} are due to CH stretching and are due to residual epoxy that was used in preparation of sample chips. SQW-115 (Fig. 7c) shows small, sharp OH bands at 3600 and 3700 cm^{-1}. Bands at ~3700 cm^{-1} are commonly associated with alteration products such as layer silicates (Johnson and Rossman, 2003) so the actual water content may be lower. In addition, the traces of epoxy also contain OH and may contribute to estimates of water content. However, we have selected spectra for analysis with little or no epoxy, as judged by their small CH absorption bands. Plagioclase water contents of the mafic granulites vary from 7 to 317 ppm H2O (7×10^{-4} – 3.2×10^{-2} wt%), and they are much larger in the felsic granulite, from 151 to 4178 ppm H_2O (1.5×10^{-2} – 4.2×10^{-1} wt%) (Table 2). Thus, our results indicate that plagioclase is dry in the mafic granulites, while it is variably dry to moderate in the felsic granulite.

4.5 Grain size and differential stress

Grain size was analyzed in six lower crustal xenoliths and one upper mantle xenolith. Grain size distribution plots are shown in Figure S5. In the following, mean grain size refers to the arithmetic mean of the grain size distribution, corrected for the two-dimensional sectioning of the grains. Because of the lack of monophase domains of plagioclase and clinopyroxene in granulites SQL-48, SQW-76, and SQW-115, grain sizes in these xenoliths were determined from polyphase domains and were not used for estimating the differential stress. The grain size distributions of plagioclase and clinopyroxene are unimodal, with means of the distributions ranging from 346 to 482 μm for plagioclase and from 354 to 500 μm for clinopyroxene (Fig. S5). Thus, the mean grain size of plagioclase and clinopyroxene is similar in the polyphase domains.

Differential stress was estimated based on the grain size in monophase plagioclase and clinopyroxene domains present in three mafic granulite xenoliths (SQ-16, SQW-75 and SQW-110). The monophase domains in two xenoliths (SQW-75 and SQW-110) show unimodal grain size distributions (Fig. S5); the mean grain size of the unimodal distributions is 454−528 μm for plagioclase and 256 μm for clinopyroxene. These mean grain sizes correspond to differential stress of 12–13 MPa for plagioclase and 20 MPa for clinopyroxene (Table 1). Bimodal distributions of both plagioclase and clinopyroxene grain sizes are observed in xenolith SQ-16 (Fig. S5). The small plagioclase (d < 330 μm) and clinopyroxene (d < 148 μm) grains of the bimodal distributions occur as clusters of recrystallized grains either along the boundaries or within the areas of three and quadruple junctions between porphyroclasts. The differential stress estimated based on the mean grain size of the recrystallized plagioclase (d = 122 μm) and clinopyroxene (d = 83 μm) grains is 33 MPa and 70 MPa, respectively. We note that the solid pressure medium apparatus with a talc assembly used in the deformation experiments of Avé Lallement (1978) for the clinopyroxene paleopiezometer calibration may overestimate flow stress about 130% to more

Solid Earth Discuss., doi:10.5194/se-2017-45, 2017
Manuscript under review for journal Solid Earth
Discussion started: 11 May 2017
© Author(s) 2017. CC-BY 3.0 License.

than 150% (Green and Borch, 1989; Stewart et al., 2013). Thus, the reported differential stresses for clinopyroxene may significantly overestimate the true flow stress.

To further constrain differential stress, we analyzed the grain size and subgrain size of olivine composing a monomineralic lens in xenolith SQ-16 (Fig. S5). The mean olivine grain size is 340 μm, which corresponds to a differential stress of 17 MPa (Table 1). The differential stress calculated from the mean olivine subgrain size (217 μm) is 7 MPa using the subgrain size paleopiezometer of Toriumi (1979). The subgrain size of olivine is similar to that of plagioclase (228 μm) and clinopyroxene (215 μm) in the same xenolith (SQ-16).

The lherzolite xenolith SQ-68 is characterized by alternation of monophase olivine layers and polyphase olivine + orthopyroxene + clinopyroxene layers. Both types of layers have unimodal olivine grain size distributions (Fig. S5). Based on the mean olivine recrystallized grain size (361 μm) in monophase olivine domains we estimated a differential stress of 17 MPa using the paleopiezometric calibrations of Van der Wal et al. (1993) (Table 1). Olivine has a subgrain size of 236 μm, which corresponds to a differential stress of 6 MPa. The mean olivine grain size for the polyphase domains is 163 μm.

4.6 Crystallographic preferred orientations

We examined the bulk CPOs of plagioclase, clinopyroxene, orthopyroxene and olivine in six granulites and one lherzolite (Fig. 8). In granulites SQ-16, SQW-75, and SQW-110 and the lherzolite SQ-68, CPOs of plagioclase, clinopyroxene, and olivine monophase domains were analyzed, while in the granulites SQL-48, SQW-76, and SQW-115 CPOs were examined in polyphase domains. In one case (SQ-16), we analyzed the plagioclase and clinopyroxene CPOs in different monophase domains within the same thin section to explore the contribution of each domain to the bulk crystallographic texture (Fig. 9). In the following we use the convention that parentheses (hkl) indicate planes and square brackets [uvw] indicate axes.

4.6.1 Plagioclase

Plagioclase has a weak to moderate CPO with J-index ranging from 2.4 to 4.7. The weak plagioclase CPO is also exhibited by the distributions of the uncorrelated misorientation angles, which generally follow the theoretical random distribution (Fig. S6). Although there is significant variation and scatter in the CPOs, plagioclase crystallographic orientations in four xenoliths (SQ-16, SQL-48, SQW-75, and SQW-76) tend to show a maximum of [100] axes subparallel to the lineation (Fig. 8a). The poles to the (010) and/or (001) planes tend to be grouped into point maxima oriented subparallel to the pole to foliation. This CPO is consistent with deformation being accommodated primarily by activation of the (010)[100] and (001)[100] slip systems. The (010)[100] and (001)[100] slip systems have been reported as primary plagioclase slip systems in naturally and experimentally deformed rocks (Ji and Mainprice, 1988; Ji et al., 2000, 2004; Xie et al., 2003; Gómez Barreiro et al., 2007; Mehl and Hirth, 2008; Hansen et al., 2013). One of the xenoliths (SQW-75) with high concentration of [100] subparallel to the lineation, is characterized by [001] axes distributed along a girdle oriented at high angle to the lineation (Fig. 8a). The orientation of [010] axes is dispersed leading to a more complex distribution. The plagioclase CPO in this xenolith may be classified as an axial-[100] type (axial-A CPO of Satsukawa et al., 2013). The axial-[100] CPO symmetry is consistent with the activation of the (010)[100] and (001)[100] plagioclase slip systems, and may be associated with prolate shape fabric geometry (Satsukawa et al., 2013). Two xenoliths (SQW-110, and SQW-115) have (010) planes and [001] directions parallel to the foliation plane and lineation, respectively (Fig. 8a). The [100] axes show concentrations within or close to the foliation plane and at high angle to the lineation. This CPO pattern corresponds to the type-C plagioclase CPO of Ji et al. (2014), which is characteristic of plastically deformed mafic rocks. Type-C CPO indicates the dominance of (010)[001] plagioclase slip system. Activation of the (010)[001] slip system is commonly identified in naturally and experimentally deformed plagioclase (Ji and Mainprice, 1988; Kruse et al., 2001; Stünitz et al., 2003).

All granulite xenoliths show strong preferred orientations of low angle (2–10°) misorientation axes, clustered subparallel to [-100] axes (Fig. 8a). This observation is consistent with tilt subgrain boundaries in (010) built of (010)[001]

Solid Earth Discuss., doi:10.5194/se-2017-45, 2017
Manuscript under review for journal Solid Earth
Discussion started: 11 May 2017
© Author(s) 2017. CC-BY 3.0 License.

edge dislocations. The correlated misorientation angle distributions are non-random, and exhibit peaks at <10°, which manifests the predominance of subgrain boundaries in plagioclase (Fig. S6). The second peak at 180° represents twinning.

4.6.2 Clinopyroxene

Clinopyroxene CPO has similar low strength to the plagioclase CPO, with the J-index ranging from 2.5 to 4.4 and uncorrelated misorientation angle distributions largely following the theoretical random distributions (Fig. S6). Clinopyroxene crystallographic orientations tend to show the [100] or [001] axes oriented roughly parallel to the lineation and a high concentration of the poles to the (010) plane oriented subparallel to the pole to foliation (Fig. 8b). The observed CPO patterns indicate activation of the (010)[100] and (010)[001] slip systems. Numerical simulations show that (010)[100] and (010)[001] are important slip systems for clinopyroxene CPO development (Ulrich and Mainprice, 2005). Clinopyroxene CPO patterns in the studied granulites do not support the activation of (100)[001] slip system, commonly reported in experimental deformation studies (Kirby and Christie, 1977; Avé Lallemant, 1978; Kirby and Kronenberg, 1984). In two xenoliths (SQL-48, and SQW-75) the poles to the (010) plane form girdles at high angle to the lineation and [100] axes are subparallel to the lineation (Fig. 8b). This CPO pattern has an axial-[100] symmetry but differs from the clinopyroxene L-type pattern (Helmstaedt et al., 1972; Ulrich and Mainprice, 2004) in that [100] axes, instead of [001] axes, are parallel to the lineation.

4.6.3 Orthopyroxene

Orthopyroxene exhibits a weak to moderate CPO with the J-index ranging from 2.0 to 4.8. The small number of grains (<200) present in sample SQW-115 may have resulted in overestimation of the CPO strength for this xenolith (J = 6.4). Orthopyroxene shows a variety of CPO types in the analyzed granulites (Fig. 8c). In two samples (SQW-76, and SQW-115), the [100] axes are roughly normal to the foliation plane and the [001] axes are subparallel to the lineation. This type of texture is indicative for deformation with dominant glide on the (100)[001] system and is frequently seen in naturally deformed orthopyroxene (Nicolas and Poirier, 1976; Vauchez et al., 2005; Jung et al., 2010; Soustelle et al., 2010). Three xenoliths (SQ-16, SQW-75, and SQW-110) tend to show the [100] and/or [001] axes oriented subparallel to the lineation and [010] maxima oriented subparallel to the pole to foliation (Fig. 8c). The observed CPO patterns indicate activation of the (010)[100] and (010)[001] slip systems. Glide on the (010)[001] slip system has been documented in naturally deformed orthopyroxene (Hidas et al., 2007; Jung et al., 2010), but alignment of [100] axes with the lineation is not commonly observed. Low-angle misorientation axes in orthopyroxene crystals are abundant and exhibit predominance of [010] rotation axes. This CPO distribution is consistent with subgrain boundaries being predominantly built out of (100)[001] edge dislocations.

4.6.4 Olivine

We examined olivine CPO from a monomineralic lens in granulite xenolith SQ-16 (Fig. 8d) and the upper mantle lherzolite. Olivine in both the granulite and the lherzolite has a moderately strong CPO with J-index being 4.0 and 4.4, respectively. Olivine in the granulite xenolith exhibits a CPO with [100] subparallel to the lineation, and both [010] and [001] almost perpendicular to the lineation (Fig. 8d). The [010] axes also show a high concentration within the foliation plane, at high angle to the lineation. This distribution of olivine crystallographic orientations is intermediate between an A-type and E-type CPO pattern (Jung and Karato, 2001). The bulk olivine texture in the lherzolite xenolith SQ-68 has previously been described by Palasse et al. (2012; fig. 4a). Olivine exhibits a strong CPO with pattern intermediate between A-type and axial-[100]. Here, we focus on olivine CPO in the monophase domain from which we estimated the differential stress. Olivine crystallographic orientations exhibit an axial-[100] symmetry, characterized by point concentrations of [100] near

Solid Earth Discuss., doi:10.5194/se-2017-45, 2017
Manuscript under review for journal Solid Earth
Discussion started: 11 May 2017
© Author(s) 2017. CC-BY 3.0 License.

the lineation and distributions of [010] and [001] axes along girdles at high angle to the lineation (Fig. 8d). The axial-[100] CPO indicates activation of the {0kl}[100] slip systems and may be associated with constrictional strain (Tommasi et al., 1999; Chatzaras et al., 2016) and high stress (Carter and Avé Lallemant, 1970; Jung and Karato, 2001).

In both xenoliths, low-angle misorientation axes describing olivine subgrain boundaries show girdle distributions between [001] and [010] with a prominent maximum parallel to [010]. This distribution of misorientation axes is expected for subgrain boundaries built from {0kl}[100] edge dislocations, with predominant contribution of (001)[100] dislocations. It is striking that olivine misorientation axes distributions in the granulite and the lherzolite are similar, indicating that subgrain boundary formation was accommodated by dislocations with similar slip systems. The high proportion of low-angle (<10°) correlated misorientation angles of both granulite and lherzolite (Fig. S6) highlights the abundance of subgrain boundaries in both rocks.

4.6.5 Domainal crystallographic preferred orientations

The weak to moderate CPO of plagioclase and clinopyroxene could be the result of either consistently weak CPO throughout the analyzed samples or the combination of moderate to strong but variable CPOs in different parts of the samples. To distinguish between the two possibilities, we compared the plagioclase (P) and clinopyroxene (C) CPO patterns among different domains of xenolith SQ-16 (Fig. 9a). Domains P1, C1 and P2, C2 have their boundaries parallel and oblique (~45°) to the main granulite foliation, respectively. The boundaries of domains P2 and C2 are parallel to the trace of a zone of localized shearing, which causes the displacement observed between the clinopyroxene domains C1 and C2.

We observe a strong correlation between the orientations of crystallographic axes and the orientations of the domain boundaries. Plagioclase in domain P1 tends to show an alignment of [100] axes within the foliation plane, with maxima subparallel to the lineation (Fig. 9b). Clinopyroxene in C1 also exhibits maxima of [001] axes and poles to (010) planes subparallel and at high angle to the lineation, respectively (Fig. 9c). In domains P2 and C2, both minerals exhibit maxima of (010) planes and [100] axes parallel to the domain boundaries. The domainal CPOs of plagioclase (J-index of 5.5 and 6.8) and clinopyroxene (J-index of 3.3 and 6.9) are stronger compared to the bulk CPOs. Our observations indicate that the weak plagioclase and clinopyroxene bulk CPOs in granulite SQ-16 result from the combination of strong but inconsistent CPOs in different parts of the xenolith.

5 Discussion

5.1 Tectonic context of the San Quintin xenoliths

The complex tectonic evolution of the Pacific-North American plate boundary makes it difficult to assess the snapshot of the plate boundary evolution for which the San Quintin xenoliths provide constraints. Because the basalts of the San Quintin volcanic field erupted recently (Pleistocene to less than 5,000-6,000 years ago), the entrained peridotite xenoliths are interpreted to provide information for the "present" mechanical properties and composition of the upper mantle beneath the northwest part of the Baja California microplate (Cabanes and Mercier, 1988; Palasse et al., 2012). These studies attribute the strong deformation of the upper mantle xenoliths to shearing along either a lithospheric-scale transcurrent shear zone or a sub-horizontal shear zone in the shallow mantle, which decouples the deeper mantle from the lower crust of the Baja California microplate. In both cases, deformation in the upper mantle xenoliths may be associated with the relative motion between the northern Baja California microplate and the Pacific plate (Plattner et al., 2007, 2009).

For the crustal xenoliths there is larger uncertainty regarding the snapshot of the plate boundary deformation history they capture and which crustal level they represent (Griffin and O'Reilly, 1987; Rudnick, 1992; Downes, 1993). The metamorphic conditions (T = 751 ± 27 – 886 ± 87 °C and P = 300 – 600 MPa) estimated from the San Quintin granulite xenoliths correspond to the uppermost lower crust (depths of 15–22 km) in the northern Baja California lithosphere.

© Author(s) 2017. CC-BY 3.0 License.

Combining the microstructural information, geothermometry and pseudosections, the overall P-T path of the San Quintin granulite xenoliths may be described from the following two stages. The first stage involves emplacement of gabbros in the deep crust, possibly intruding and heating earlier metabasites that were metamorphosed to two-pyroxene granulites; cooling from high T is shown by the orthopyroxene rims around olivine, crystallisation of melt pockets and pyroxene exsolution. The second stage involves decompression to ~300-500 MPa, resulting in local symplectites. Deformation is likely to have operated at a late stage of the first event, as the symplectites and fine-grained melt pockets are undeformed, in contrast to orthopyroxene in the rims around olivine, which includes evidence of intragrain deformation.

We consider two possible end member scenarios for the origin of the San Quintin crustal xenoliths. In the first scenario, the xenoliths formed in the shallow lower crust of the Mesozoic western Peninsular Ranges Batholith, and were tectonically emplaced at shallower crustal levels prior to eruption and xenolith capture. In the second scenario, the xenoliths sample the uppermost lower crust in the active boundary between the Pacific plate and Baja California microplate.

In the first scenario, crustal and mantle xenoliths provide constraints for different snapshots of the plate boundary evolution. Granulites are interpreted to be associated with the Mesozoic Peninsular Ranges Batholith magmatic arc while the upper mantle xenoliths are interpreted to record active processes beneath Baja California peninsula. The equilibrium temperatures estimated from the granulite xenoliths are 200–300 °C higher compared to the temperatures predicted from the maximum background geotherm for the magmatic arc (Rothstein and Manning, 2003) (dark blue curve in Fig. 10). This difference could be the result of transient heating during pluton emplacement (Barton et al., 1988). The granulites may have been tectonically emplaced at shallower crustal levels (i.e. middle or upper crust) soon after the cessation of their ductile deformation and prior to their entrainment. Prolonged "residence" of granulites at high temperatures would obliterate any intragrain deformation and dynamic recrystallization features such as subgrain boundaries, undulose extinction, and lobate grain boundaries observed in the analyzed xenoliths. Thus, in the first scenario, the gabbroic and granulite outcrops must have existed in the upper crust and ~~that~~ the xenolith entrainment occurred at this crustal level. Gabbros are locally present in the western Peninsular Ranges Batholith; mafic plutonic rocks outcrop 20 km east of the San Quintin volcanic field (Gastil et al., 1975; Schmidt et al., 2014). It is therefore possible that the gabbroic xenoliths comprise entrained fragments of the western Peninsular Ranges Batholith. To the best of our knowledge, no granulite exposures have been reported in Baja California peninsula so far.

In the second scenario, xenoliths record active processes in the boundary between the Pacific plate and the Baja California microplate. A geothermal gradient of 40 °C/km fits well with the distribution of equilibrium conditions in the studied granulite xenoliths (broken red line in Fig. 10), and may describe the present geotherm beneath northwest Baja California. The studied granulites have a similar range of equilibrium temperatures as the porphyroclastic and mosaic upper mantle xenoliths (Cabanes and Mercier, 1988), implying near-isothermal conditions in the lower crust beneath the San Quintin volcanic field (Fig. 10). The observed thermal structure of the lithosphere could correspond to a quasi-steady-state geotherm reflecting long-lived plutonism (Depine et al., 2008). Important for the development of near-isothermal conditions in the crust are the existence of elevated heat fluxes from the mantle and melt focusing (Depine et al., 2008). Luhr et al. (1995) argued that partial melting occurs at unusually shallow mantle levels beneath the San Quintin volcanic field. High mantle heat flux leading to melting may be associated with the inferred slab window beneath northern Baja California peninsula. The suggested location of the slab window correlates well with the location of the San Quintin volcanic field (Paulssen and De Vos, 2016). Focused asthenospheric upwelling within the slab window and strike-slip shearing in a lithospheric-scale, transcurrent shear zone (e.g., the Baja California shear zone) can both result in melt focusing (e.g., Thorkelson and Breitsprecher, 2005; Cao and Neubauer, 2016). Thus, the interpretation of the granulite xenoliths as being derived from the modern uppermost lower crust beneath northwest Baja California fits well with the active tectonic processes at the plate boundary.

Solid Earth Discuss., doi:10.5194/se-2017-45, 2017
Manuscript under review for journal Solid Earth
Discussion started: 11 May 2017
© Author(s) 2017. CC-BY 3.0 License.

The entrained crustal xenoliths, which range from undeformed gabbros to strongly deformed granulites, could define a horizontal strain gradient in the uppermost lower crust. In support of the existence of a horizontal strain gradient is the fact that gabbroic xenoliths are predominantly present in the Media Luna volcanic complex while granulites in the Woodward volcanic complex, with the two complexes being 3 km apart. Alternatively, the two volcanic complexes may sample different crustal levels. To explain the strongly deformed mosaic lherzolite xenoliths as opposed to the less deformed coarse granular and porphyroclastic xenoliths, Cabanes and Mercier (1988) suggested the existence of a shear zone in the upper mantle beneath the San Quintin volcanic field. The upper mantle xenolith (SQ-68) studied in this work has an equigranular mosaic microstructure (Palasse et al., 2012), and therefore could sample this upper mantle shear zone. We therefore suggest that the strongly deformed granulites and lherzolites entrained in the San Quintin basalts sample different levels of a lithospheric-scale, wrench shear zone. Such a major shear zone could comprise a strand of the active BCSZ, which accommodates the relative movement between the Pacific plate and the Baja California microplate (Fig. 1).

Plagioclase and olivine CPOs provide further support to the interpretation that the San Quintin xenoliths may record active processes beneath the northwest Baja California microplate, as the fabrics are consistent with transtensional deformation. Plagioclase in the granulite xenolith SQW-75 and olivine in the lherzolite xenolith SQ-68 exhibit CPO of axial-[100] symmetry (Fig. 8a, d). The axial-[100] CPO symmetry in both minerals has been attributed to deformation producing prolate shape fabric geometries (Tomassi et al., 1999; Satsukawa et al., 2013; Chatzaras et al., 2016). Wrench-dominated transtension in Baja California (Legg et al., 1991; Umhoefer, 2011) could have induced constrictional strain in both the upper mantle and crust, leading to the formation of the observed axial-[100] CPO symmetries. Clinopyroxene also exhibits CPO patterns with axial-[100] symmetry (SQW-75 and SQL-48), which could be the result of constriction, as well. However, it is the axial-[001] rather than axial-[100] symmetry, which has been associated with linear fabric geometries in clinopyroxene (Helmstaedt et al., 1972; Ulrich and Mainprice, 2004).

To summarize, the San Quintin granulite xenoliths formed at lithospheric depths corresponding to the uppermost lower crust. Ductile deformation of the granulites took place after cooling from the maximum P-T conditions and prior to symplectite and melt formation. Thus, deformation conditions range $700 < T < 890$ °C and $370 < P < 580$ MPa. The granulite xenoliths may sample either the Mesozoic Cordilleran magmatic arc or a lithospheric-scale shear zone in the active Pacific-Baja California plate boundary. Although we cannot exclude the former, we consider the latter as the most likely tectonic scenario.

5.2 Deformation mechanisms in Baja California lithosphere

We interpret the microstructures observed in the San Quintin granulite and lherzolite xenoliths to show deformation by a combination of dislocation creep and grain boundary sliding. Plagioclase and clinopyroxene, which are the major rock forming minerals in the studied granulites, exhibit evidence for deformation by both grain size insensitive and grain size sensitive deformation mechanisms. Evidence for intragrain deformation by dislocation creep includes: 1) phase segregation and formation of compositional layering (Kenkmann and Dresen, 2002); 2) undulose extinction of porphyroclasts; 3) high amount of low-angle (<10°) misorientation angles between subgrain boundaries; and 4) the large number of low-angle misorientation axes with strongly clustered distributions (Fliervoet et al., 1999). Furthermore, dynamic recrystallization accommodated by subgrain rotation recrystallization is inferred from microstructures such as: 1) subgrains with sizes similar to the sizes of the recrystallized grains; 2) recrystallized grains lacking significant internal deformation; 3) recrystallized grains with twins oriented at low angle to the twins in adjacent porphyroclasts; and 4) core-and-mantle structures (e.g., Drury and Urai, 1990). Recrystallization, accommodated by grain boundary migration, is inferred from interpenetrating grain boundaries (Drury and Urai, 1990). Thus, dislocation processes and dynamic recrystallization have contributed substantively to the total deformation of the mafic granulites.

© Author(s) 2017. CC-BY 3.0 License.

Grain boundary sliding may have also been an important mechanism in the deformation of the lower crustal xenoliths. Quadruple junctions associated with straight and aligned grain boundaries (Figs. 2e, f and 3c) comprise a transitional configuration of grain boundaries between two low energy, and therefore thermodynamically stable, triple junction configurations (Ashby and Verrall, 1973). This grain boundary readjustment is accommodated by translation of grains past each other by sliding along their boundaries. Boundaries of plagioclase grains aligned with twin boundaries (Fig. 3d) are interpreted as micro-shear zones (sensu Bons and Jessell, 1999), which preferentially localize shear along grain boundaries and intragrain easy slip planes. Deformation in micro-shear zones may cause localized movement of dislocations and development of subgrain boundaries near and subparallel to the grain boundaries (Fig. 3b) (Drury and Humphreys, 1988; Ree, 1994). Given the strong evidence for dislocation creep, the most likely process that accommodated grain boundary sliding was the movement of dislocations rather than grain boundary diffusion.

A common microstructure in the studied granulites is the development of 120° triple junctions between grains characterized by limited intragrain deformation and straight, or smoothly curved, grain boundaries (Fig. 3c). This microstructure has been attributed to grain boundary re-organization to low energy triple junctions at high temperature conditions (Gottstein and Shvindlerman, 2000; Piazolo et al., 2002). Such an interpretation is consistent with the high-temperature deformation estimated for the San Quintin granulite xenoliths.

The cooperation of grain size sensitive and insensitive processes can also be inferred from the analysis of the CPOs and misorientation distributions. The weak to moderate bulk CPOs (Fig. 8), and the distributions of the uncorrelated misorientation angles, which follow the theoretical distribution for a random CPO (Fig. S6), may indicate a transition to diffusion creep. On the other hand, the large number of low-angle misorientation axes and their non-random distributions (Fig. S6), imply deformation by dislocation creep. Further support for the latter argument comes from the detailed analysis of CPO in granulite SQ-16. In contrast to the bulk CPO, the domainal CPOs are strong (J-index two to three times higher compared to the bulk CPO) and variable among the different domains (Fig. 9). This observation implies that the weakness of the bulk CPO may not always be indicative of grain size sensitive processes; rather, it could be produced by the combination of strong domainal CPOs with variations in the topology of their crystallographic axis distributions.

The development of strong domainal CPOs can be attributed either to host control or to kinematic control. In the first case, a very strong CPO is inherited from a pre-existing grain (e.g., porphyroclast) and is subsequently weakened due to transition in the dominant operating deformation mechanism from dislocation creep to a grain size sensitive mechanism that involves grain boundary sliding (Jiang et al., 2000; Skemer and Karato, 2008). In the second case, the CPO reflects the local flow field produced by flow heterogeneities (Bestmann et al., 2006; Mehl and Hirth, 2008). We argue that the CPOs formed in different domains of granulite SQ-16 are kinematically controlled and reflect the local flow field. Our interpretation is based on: 1) the correlation between the concentrations of plagioclase and clinopyroxene crystallographic axes and the orientations of the local kinematic axes e.g., foliation trace near the zone of localized shearing (domains P2 and C2 in Fig. 9); and 2) the back-rotation of the poles to (010) planes in plagioclase relative to the sense of shear on the zone of localized shearing (domain P2 in Fig. 9b). In agreement with the deformation experiments of Gómez Barreiro et al. (2007), the development of (010) maxima inclined against the shear sense and at high angles to the local shear plane is associated with dominant (010)[100] slip and subsidiary (010)[001] and (001)[100] slip. The activity of these slip systems is observed in the majority of the San Quintin granulite xenoliths. At high-temperature deformation, the (010)[100] and (010)[001] have been recognized as the primary slip systems in plagioclase (Olsen and Kohlstedt, 1984; Ji and Mainprice, 1990; Stünitz et al., 2003; Mehl and Hirth, 2008). Thus, deformation in the granulite xenoliths involved dislocation glide on the easiest slip system(s). Deformation by combination of dislocation creep and grain boundary sliding has also been described in the San Quintin upper mantle xenoliths (Palasse et al., 2012) and is further supported by our microstructural observations.

To summarize, microstructural evidence suggests that the mafic granulite and lherzolite xenoliths deformed by a combination of dislocation creep and grain boundary diffusion-controlled creep, where both mechanisms operate together.

Solid Earth Discuss., doi:10.5194/se-2017-45, 2017
Manuscript under review for journal Solid Earth
Discussion started: 11 May 2017
© Author(s) 2017. CC-BY 3.0 License.

A mechanism that has possibly contributed to deformation in the San Quitnin xenoliths is dislocation-accommodated grain boundary sliding. This mechanism is increasingly recognized as an important deformation process in both plagioclase-rich rocks (Kenkmann and Dresen, 2002; Svahnberg and Piazolo, 2010; Hansen et al., 2013; Miranda et al., 2016) and olivine-rich rocks (Hirth and Kohlstedt, 1995; Warren and Hirth, 2006; Drury et al., 2011; Hansen et al., 2011; Precigout and Hirth, 2014; Chatzaras et al., 2016). The large grain sizes in the San Quintin xenoliths imply that dislocation creep is the dominant deformation mechanism. However, the high homologous temperatures estimated in the mafic granulites facilitate the transition to diffusion creep at larger, than the expected, grain sizes. The presence of melt in the Baja California lithosphere (Basu, 1977; Cabanes and Mercier, 1988; Luhr et al., 1995; Luhr and Aranda-Gómez, 1997; Palasse et al., 2012; this study) may also influence rock deformation behavior by enhancing grain boundary diffusion and grain boundary sliding (de Kloe et al., 2000; Holtzman et al., 2003; Tommasi et al., 2004; Palasse et al., 2012). Assuming that the San Quintin crustal xenoliths record active deformation in the Pacific plate-Baja California microplate boundary, deformation in both the uppermost lower crust and upper mantle is accommodated by a combination of dislocation creep and diffusion creep processes.

5.3 Strength profile of a strike-slip plate boundary

The critical result from the San Quintin xenoliths is that the shear stress in the uppermost lower crust, as estimated for plagioclase (6–17 MPa for plagioclase), overlaps with the stress of the upper mantle (9 MPa) (Fig. 11a); shear stress is calculated assuming strike-slip deformation. The similar strength between the two lithospheric levels is also suggested by the same differential stress (~17 MPa) in both the olivine lens in the granulite xenolith and olivine in the lherzolite xenolith. The determined upper mantle strength is consistent with the results of recent studies of upper mantle xenoliths from two other areas of the Pacific-North American plate boundary, the Coyote Lake volcanic field in the San Andreas Fault system (Titus et al., 2007; Chatzaras et al., 2015), and the Cima volcanic field, situated east of the eastern California Shear zone (Behr and Hirth, 2014). The stresses recorded in the San Quintin upper mantle xenolith is directly comparable to the cumulative range of the calculated differential stresses (10–18 MPa) from the San Andreas Fault system and the Cima xenoliths (Behr and Hirth, 2014; Chatzaras et al., 2015). Furthermore, shear stress in the uppermost lower crust beneath San Quintin is similar to the shear strength of the San Andreas Fault (10–17 MPa) in the upper crust, constrained from frictional properties of the San Andreas Fault Observatory at Depth core samples (Lockner et al., 2011; Carpenter et al., 2012) (Fig. 11a).

The strength profile in Fig. 11a does not support a “jelly sandwich” or a “crème brûlée" model for the lithospheric strength of the strike-slip plate boundary. The jelly sandwich model requires a strong upper mantle, while the crème brûlée model assumes that crust comprises the load-bearing layer within the lithosphere (Brace and Kohlstedt, 1980; Chen and Molnar, 1983; Jackson, 2002; Burov and Watts, 2006). Combining the observations from the Baja California Shear Zone, the San Andreas Fault system, and the Eastern California Shear Zone, we suggest that lithospheric strength in the upper crust, uppermost lower crust, and uppermost mantle in major strike-slip fault zones may be low (between 6 and 17 MPa) and constant with depth. Interestingly, Plattner et al. (2009) show that a shear stress of 10 MPa on the San Benito–Tosco Abreojos fault, which is part of the BCSZ, explains better the observed geodetic motion of the Baja California microplate. This result further supports the suggestion for a low strength of the Pacific-Baja California plate boundary and implies that the San Quintin xenoliths may constrain deformation processes in the active plate boundary.

5.4 Viscosity structure of a strike-slip plate boundary

To describe the rheological structure of the boundary between the Pacific plate and the Baja California microplate, we quantify the rheological properties of the lithosphere beneath the San Quintin volcanic field combining microstructural constraints with laboratory-derived flow laws. Figure 11 describes the variation of strain rate and viscosity as a function of

Solid Earth Discuss., doi:10.5194/se-2017-45, 2017
Manuscript under review for journal Solid Earth
Discussion started: 11 May 2017
© Author(s) 2017. CC-BY 3.0 License.

depth based on the xenolith constraints for the shallow lower crust and upper mantle. To calculate strain rate, we use the experimentally derived flow law:

$$\dot{\varepsilon} = A\sigma^n d^{-m} exp\left(\frac{-Q}{RT}\right) \quad (2)$$

where $\dot{\varepsilon}$ is the strain rate, A is a material constant, σ is the differential stress, n is the stress exponent, d is the recrystallized grain size, m is the grain-size exponent, Q is the activation energy, R is the molar gas constant, and T is the temperature. The term A can be expanded to describe the dependence of strain rate on water fugacity. Because multiple deformation mechanisms operate simultaneously, we calculate the total strain rate as the sum of strain rates due to dislocation creep (dis), diffusion creep (dif), and dislocation accommodated grain boundary sliding (disGBS) –only for the upper mantle– at the deformation temperatures estimated for the xenoliths using phase equilibria modeling and geothermometry. The constitutive relationship describing the total strain rate can be written:

$$\dot{\varepsilon}_{total} = \dot{\varepsilon}_{dis} + \dot{\varepsilon}_{dif} + \dot{\varepsilon}_{disGBS} \quad (3)$$

Our water content analysis shows that plagioclase in the mafic granulites is dry. The wet plagioclase in the felsic granulite implies heterogeneous hydration in the lithosphere beneath northern Baja California. However, the composition of xenolith SQ-76 does not allow to assess further the depths and conditions at which the observed hydration takes place. Dry olivine (0–6.6 ppm H_2O) has also been described in the upper mantle xenoliths (Peslier and Luhr, 2006). Thus, we use flow law parameters for dry plagioclase and olivine. For dry plagioclase, we use: 1) the dislocation creep and diffusion creep flow law parameters for anorthite from Rybacki and Dresen (2000); 2) the dislocation creep and diffusion creep flow law parameters for 50An/50Cpx or 75An/25Cpx, depending on the granulite modal composition (Dimanov and Dresen, 2005); and 3) the flow law derived from the experimentally deformed Pikwitonei granulite (Wilks and Carter, 1990). Microstructures in the Pikwitonei granulite imply deformation by dislocation creep and possibly diffusion accommodated grain boundary sliding (Wilks and Carter, 1990). For dry olivine, we use the dislocation creep and diffusion creep flow laws from Hirth and Kohlstedt (2003), modifying the pre-exponential constant, A, for diffusion creep based on Hansen et al. (2011). For dislocation accommodated grain boundary sliding we use the flow law from Hansen et al. (2011). Combining the differential stress and strain rate estimates we calculate the effective viscosity (η) using the relationship:

$$\eta = \frac{\sigma}{2\dot{\varepsilon}} \quad (4)$$

In Figure 11b we plot the strain rates estimated based on constraints from the San Quintin xenoliths; strain rates were calculated using the flow laws and parameters discussed above. The plagioclase flow laws from Dimanov and Dresen (2005) and Wilks and Carter (1990) yield comparable strain rates ranging from 1.2×10^{-14} to 7.3×10^{-12} s^{-1}, which are reasonable, if not low, for a shear zone active in a crust characterized by a hot geotherm (Fig. 11b). Strain rate increases with depth from 6.0×10^{-14} to 2.7×10^{-12} s^{-1} as a result of the geothermal gradient in uppermost lower crust beneath northern Baja California. Using the An100 plagioclase flow law from Rybacki and Dresen (2000), we estimate considerably lower strain rates (1.7×10^{-17} – 7.0×10^{-15} s^{-1}) for the hot crust. Such low strain rates could be representative for the internal deformation of the Baja California microplate (Plattner et al., 2007) rather than the deformation near the Pacific-Baja California plate boundary. In the upper mantle, the strain rate in the olivine monophase layer of the lherzolite xenolith from which we determined the differential stress, is 6.1×10^{-15} s^{-1}. Assuming that stress is constant between neighboring layers, we use the stress estimated from the monophase layer to constrain the strain rate of adjacent polyphase layers consisting of olivine + orthopyroxene + clinopyroxene. Because polyphase domains are volumetrically dominant in the lherzolite xenolith, we consider the associated strain rate to be more representative. In the polyphase layers, strain rate is 5.7×10^{-14} s^{-1}, and is in good agreement with the upper mantle strain rates constrained from the SAF and Cima xenoliths (Fig. 11b; Behr et al., 2014; Chatzaras et al., 2015).

Figure 11c shows the viscosity structure of the lithosphere beneath northern Baja California constrained from the San Quintin xenoliths. Also shown are viscosities estimated from the SAF and Cima xenoliths (Behr and Hirth, 2014;

Solid Earth Discuss., doi:10.5194/se-2017-45, 2017
Manuscript under review for journal Solid Earth
Discussion started: 11 May 2017
© Author(s) 2017. CC-BY 3.0 License.

Chatzaras et al., 2015). Viscosities estimated using the strain rates constrained with the flow laws from Dimanov and Dresen (2005) and Wilks and Carter (1990) decrease with depth from 1.8×10^{20} Pa s at ~18 km to 2.2×10^{18} Pa s at ~20 km as a result of the thermal structure of the lithosphere at these depths (Fig. 11c). For the near isothermal conditions inferred for the lower crust beneath the San Quintin volcanic field (Fig. 10), viscosity will remain constant (~10^{18} Pa s) with depth (broken red line in Fig. 11c). Because the dominant deformation mechanism in the northern Baja California lithosphere is transitional between dislocation creep and diffusion creep, any grain size reduction is not expected to result in a major change in strength or effective viscosity of the lower crust (De Bresser et al., 2001).

The mean estimated viscosity of the upper mantle is 1.4×10^{20} Pa s, which confirms the existence of a weak shallow mantle beneath northern Baja California (Palasse et al., 2012). To constrain the viscosity of the upper mantle we used the strain rate determined for the polyphase layers in the peridotite xenolith (Fig. 11b). Because clinopyroxene occurs at relatively small modal fractions (~7%) in the studied upper mantle xenolith, and orthopyroxene behaves as a strong phase forming porphyroclasts, we used the viscosity of olivine as a reasonable approximation for the overall viscosity of the polyphase domains. The upper mantle viscosity estimated from the San Quintin xenoliths falls within the range of viscosities constrained from the Cima xenoliths (Behr and Hirth, 2014) and overlaps with the high end of the viscosities estimated from the SAF xenoliths (Chatzaras et al., 2015) (Fig. 11c).

Our analysis shows that the northern Baja California lithosphere is mechanically stratified. The viscosity of the upper mantle is similar (~10^{20} Pa s) to the viscosity of the crust at ~18 km depth and two orders of magnitude higher from the viscosity at deeper crustal levels (Fig. 11c). This viscosity structure shows a "fake" jelly sandwich type strength distribution with depth; a weak lower crust sandwiched between less week upper mantle and uppermost lower crust. An upper mantle lid, which is essential for the jelly sandwich model (Burov and Watts, 2006), is absent from the northern Baja California lithosphere. Rather, the inferred weak lower crustal layer beneath ~20 km depth may comprise a large-scale flow zone, which acts to transfer the displacement field from the mantle to the upper crust (Teyssier and Tikoff, 1998).

5.5 Implications for the rheological behavior of the lower crust during the seismic cycle

The microstructures and paleopiezometric methods used in this work are commonly interpreted to reflect the long-term mechanical behavior of the lithosphere rather than transient deformation during seismic slip and post-seismic relaxation; see, however, Trepmann et al. (2003), Druiventak et al. (2011), and Chatzaras et al. (2015) for a different interpretation. Thus, in the seismically active boundary between the Pacific plate and Baja California microplate, the rheological constraints from the San Quintin xenoliths may be more representative of long-term creep during the interseismic period. As shown in Figure 11c, a very interesting relationship arises by comparing the viscosity structure constrained from xenoliths with the one constrained from post-seismic relaxation and post-lake filling studies for the western U.S. (Thatcher and Pollitz, 2008). The mean viscosity of the uppermost lower crust at ~18 km depth determined from the San Quintin xenoliths is similar to the mean crustal viscosity of the post-seismic relaxation studies. However, viscosities in the lower crust beneath 20 km and in the upper mantle determined from the xenoliths are reversed compared to the viscosities of the post-seismic relaxation studies. If we assume that xenoliths record long-term deformation during the interseismic period, we observe an inversion in the strength of the lower crust and upper mantle during the seismic cycle. The lower crust is stronger than upper mantle during the post-seismic relaxation period, while the upper mantle becomes stronger during the interseismic period. Thus, the mechanical behavior of the lithosphere is clearly time-dependent (Pollitz et al., 2001; Thatcher and Pollitz, 2008; Gueydan et al., 2014; Chatzaras et al., 2015).

Recently, Chatzaras et al. (2015) proposed the "lithospheric feedback" model to explain the rheological behavior of the lithosphere in the SAF system. The essence of the lithospheric feedback model is that crust and lithospheric mantle act together as an integrated system; it is the way the two lithospheric layers interact during the seismic cycle rather than their relative strength, which controls the deformation in the strike-slip plate boundary. Our work highlights the role of the lower

© Author(s) 2017. CC-BY 3.0 License.

crust in coupling deformation between the upper crust and upper mantle during the seismic cycle. Lower crust may adjust its rheology to transfer distributed displacement from the mantle to the upper crust during the interseismic period, and act as a stress guide that localizes deformation during the post-seismic relaxation period.

6 Conclusions

1. The San Quintin mafic granulite xenoliths have been extracted from the uppermost lower crust (15–22 km) beneath northern Baja California, Mexico. The equilibration conditions (T = 750–890 °C, P = 400–580 MPa) of the granulites indicate a hot geotherm of 40 °C/km for the upper 20 km of the crust. Near isothermal conditions in the deeper lower crust (20–30 km) are inferred from the similarity of the equilibration temperatures between the lower crustal and upper mantle xenoliths.
2. Deformation in the uppermost lower crust and upper mantle is accommodated by a combination of grain size sensitive and grain size insensitive creep. The dominant deformation mechanism in both lithospheric layers is transitional between dislocation creep and diffusion creep.
3. Plagioclase in the mafic granulites is dry and has been deformed at differential stresses (12–33 MPa) similar to those in the upper mantle (17 MPa).
4. The lithosphere beneath northern Baja California is characterized by a low viscosity ($<10^{21}$ Pa s). The viscosity of the lower crust ($\sim10^{18}$ Pa s) at <20 km depth is two orders of magnitude lower compared to the viscosity of the shallow upper mantle ($\sim10^{20}$ Pa s). These results indicate the lack of an upper mantle lid beneath northern Baja California, and the presence of a low-viscosity zone in the lower crust. Such lower crustal flow zone may act to transfer the displacement field from the mantle to the upper crust coupling the two lithospheric layers.
5. The viscosities of the lower crust and upper mantle may change during the seismic cycle, and the lithospheric layer with the larger viscosity may not be fixed. The lower crust is stronger during the post-seismic relaxation period while the upper mantle becomes stronger during the interseismic period and long-term deformation.

Acknowledgements

This research was supported by a Marie Curie International Outgoing Fellowship to V. Chatzaras (PIOF-GA-2012-329183) within the 7th European Community Framework Programme. We thank Asish Basu (University of Texas, Arlington) for providing samples and suggesting xenolith localities. We acknowledge Saurabh Ghanekar for assistance in the field, Gill Pennock for her help with the EBSD analyses in the EM square facility at Utrecht University, Tilly Bouten (Utrecht University) and Hans de Groot (Naturalis Leiden) for assistance with the microprobe and SEM-EDS analyses, Peter van Krieken (Utrecht University) for assistance with the FTIR analyses, and Brian Hess (University of Wisconsin-Madison) for the production of high-quality thin sections used in EBSD analysis.

References

Ashby, M. F., and Verrall, R. A.: Diffusion-accommodated flow and superplasticity. Acta Metall. Mater., 21(2), 149-163, 1973.

Atwater, T.: Plate tectonic history of the northeast Pacific and western North America, The eastern Pacific Ocean and Hawaii: Boulder, Colorado, Geol. Soc. Am., Geol. N. Am., v.N, 21-72, 1989.

Atwater, T. and Stock, J.: Pacific-North America plate tectonics of the Neogene southwestern United States: an update, Int. Geol. Rev., 40(5), 375-402, 1998.

Avé Lallemant, H. G.: Experimental deformation of diopside and websterite, Tectonophysics, 48(1-2), 1-27, 1978.

© Author(s) 2017. CC-BY 3.0 License.

Barton, M. D., Battles, D. A., Debout, G. E., Capo, R. C., Christensen, J. N., Davis, S. R., and Trim, H. E.: Mesozoic contact metamorphism in the western United States, in: Metamorphism and crustal evolution of the western United States, Ernst, W.G., Pentice Hall, Los Angeles, California, Rubey, 7, 110-178, 1988.

Basu, A. R.: Textures, microstructures and deformation of ultramafic xenoliths from San Quintin, Baja California, Tectonophysics, 43(3-4), 213-246, 1977.

Basu, A. R., Young, S. W., Suttner, L. J., James, W. C., and Mack, G. H.: Re-evaluation of the use of undulatory extinction and polycrystallinity in detrital quartz for provenance interpretation, J. Sediment. Res., 45(4), 1975.

Behr, W. M., and Hirth, G.: Rheological properties of the mantle lid beneath the Mojave region in southern California, Earth Planet. Sc. Lett., 393, 60-72, 2014.

Bestmann, M., Prior, D. J., and Grasemann, B.: Characterisation of deformation and flow mechanics around porphyroclasts in a calcite marble ultramylonite by means of EBSD analysis, Tectonophysics, 413(3), 185-200, 2006.

Bons, P.D. and Jessell, M.W.: Micro-shear zones in experimentally deformed octachloropropane, J. Struct. Geol., 21, 323-334, 1999.

Brace, W. and Kohlstedt, D.: Limits on lithospheric stress imposed by laboratory experiments, J. Geophys. Res-Sol. Ea., 85(B11), 6248-6252, 1980.

Brey, G. and Köhler, T.: Geothermobarometry in four-phase lherzolites II. New thermobarometers, and practical assessment of existing thermobarometers, J. Petrol., 31(6), 1353-1378, 1990.

Bunge, H.: Texture Analysis in Materials Science: Mathematical Methods, Elsevier, 2013.

Burov, E. and Watts, A.: The long-term strength of continental lithosphere:" jelly sandwich" or" crème brûlée"?, GSA today, 16(1), 4, 2006.

Cabanes, N. and Mercier, J.: Insight into the upper mantle beneath an active extensional zone: the spinel-peridotite xenoliths from San Quintin (Baja California, Mexico), Contrib. Mineral. Petrol., 100(3), 374-382, 1988.

Cao, S., and Neubauer, F.: Deep crustal expressions of exhumed strike-slip fault systems: Shear zone initiation on rheological boundaries, Earth-Sc. Rev., 162, 155-176, 2016.

Carpenter, B., Saffer, D., and Marone, C.: Frictional properties and sliding stability of the San Andreas fault from deep drill core, Geology, 40(8), 759-762, 2012.

Carter, N. L., and Avé Lallemant, H. G.: High temperature flow of dunite and peridotite, Geol. Soc. Am. Bull., 81(8), 2181-2202, 1970.

Chatzaras, V., Tikoff, B., Newman, J., Withers, A. C., and Drury, M. R.: Mantle strength of the San Andreas fault system and the role of mantle-crust feedbacks, Geology, 43(10), 891-894, 2015.

Chatzaras, V., Kruckenberg, S. C., Cohen, S. M., Medaris, L. G., Withers, A. C., and Bagley, B.: Axial-type olivine crystallographic preferred orientations: The effect of strain geometry on mantle texture, J. Geophys. Res-Sol. Ea., 121(7), 4895-4922, 2016.

Chen, W. P., and Molnar, P.: Focal depths of intracontinental and intraplate earthquakes and their implications for the thermal and mechanical properties of the lithosphere, J. Geophys. Res-sol. Ea., 88(B5), 4183-4214, 1983.

Connolly, J. and Petrini, K.: An automated strategy for calculation of phase diagram sections and retrieval of rock properties as a function of physical conditions, J. Metamorph. Geol., 20(7), 697-708, 2002.

De Bresser, J., Ter Heege, J., and Spiers, C.: Grain size reduction by dynamic recrystallization: can it result in major rheological weakening?, int. J. Earth. Sci., 90(1), 28-45, 2001.

De Kloe, R., Drury, M. R., and Van Roermund, H. L. M.: Evidence for stable grain boundary melt films in experimentally deformed olivine-orthopyroxene rocks, Phys. Chem. Miner., 27(7), 480-494, 2000.

© Author(s) 2017. CC-BY 3.0 License.

775 DeMets, C.: A reappraisal of seafloor spreading lineations in the Gulf of California: Implications for the transfer of Baja California to the Pacific Plate and estimates of Pacific-North America motion, Geophys. Res. Lett., 22(24), 3545-3548, 1995.

Depine, G. V., Andronicos, C. L., and Phipps-Morgan, J.: Near-isothermal conditions in the middle and lower crust induced by melt migration, Nature, 452(7183), 80-83, 2008.

780 Dickinson, W. R.: Tectonic implications of Cenozoic volcanism in coastal California, Geol. Soc. Am. Bull., 109(8), 936-954, 1997.

Dimanov, A., and Dresen, G.: Rheology of synthetic anorthite-diopside aggregates: Implications for ductile shear zone, J. Geophys. Res-sol. Ea., 110(B7), 2005.

Dixon, T. H., Miller, M., Farina, F., Wang, H., and Johnson, D.: Present-day motion of the Sierra Nevada block and some

785 tectonic implications for the Basin and Range province, North American Cordillera, Tectonics, 19(1), 1-24, 2000.

Dixon, T. H., Norabuena, E., and Hotaling, L.: Paleoseismology and Global Positioning System: Earthquake-cycle effects and geodetic versus geologic fault slip rates in the Eastern California shear zone, Geology, 31(1), 55-58, 2003.

Downes, H.: The nature of the lower continental crust of Europe: petrological and geochemical evidence from xenoliths, Phys. Earth Planet. Inter., 79(1-2), 195-218, 1993.

790 Druiventak, A., Trepmann, C. A., Renner, J., and Hanke, K.: Low-temperature plasticity of olivine during high stress deformation of peridotite at lithospheric conditions—An experimental study, Earth Planet. Sc. Lett., 311(3), 199-211, 2011.

Drury, M. R., and Humphreys, F. J.: Microstructural shear criteria associated with grain-boundary sliding during ductile deformation, J. Struct. Geol., 10(1), 83-89, 1988.

795 Drury, M. R., and Urai, J. L.: Deformation-related recrystallization processes, Tectonophysics, 172(3-4), 235-253, 1990.

Drury, M. R., Lallemant, H. A., Pennock, G. M., and Palasse, L. N.: Crystal preferred orientation in peridotite ultramylonites deformed by grain size sensitive creep, Étang de Lers, Pyrenees, France, J. Struct. Geol., 33(12), 1776-1789, 2011.

Fletcher, J. M. and Munguia, L.: Active continental rifting in southern Baja California, Mexico: Implications for plate motion partitioning and the transition to seafloor spreading in the Gulf of California, Tectonics, 19(6), 1107-1123, 2000.

800 Fletcher, J. M., Kohn, B. P., Foster, D. A., and Gleadow, A. J.: Heterogeneous Neogene cooling and exhumation of the Los Cabos block, southern Baja California: Evidence from fission-track thermochronology, Geology, 28(2), 107-110, 2000.

Fliervoet, T. F., Drury, M. R., and Chopra, P. N.: Crystallographic preferred orientations and misorientations in some olivine rocks deformed by diffusion or dislocation creep, Tectonophysics, 303(1), 1-27, 1999.

Freed, A. M. and Bürgmann, R.: Evidence of power-law flow in the Mojave desert mantle, Nature, 430(6999), 548-551,

805 2004.

Gastil, R. G.: Plutonic zones in the Peninsular Ranges of southern California and northern Baja California, Geology, 3(7), 361-363, 1975.

Gastil, R. G. and Miller, R. H.: The Prebatholithic Stratigraphy of Peninsular California, vol. 279, Geol. Soc. Am., 1993.

Gastil, R. G., Phillips, R. P., and Allison, E. C.: Reconnaissance geology of the state of Baja California, Geol. Soc. Am.

810 Mem., 140, 1-201, 1975.

Gómez Barreiro, J., Lonardelli, I., Wenk, H. R., Dresen, G., Rybacki, E., Ren, Y., and Tomé, C. N.: Preferred orientation of anorthite deformed experimentally in Newtonian creep, Earth Planet. Sci. Lett., 264 (2007), 188–207, 2007.

Gottstein, G. and Shvindlerman, L. S.: Triple junction drag and grain growth in 2D polycrystals, Acta Materialia, 50, 703-713, 2000.

815 Griffin, W. and O'Reilly, S. Y.: Is the continental Moho the crust-mantle boundary?, Geology, 15(3), 241-244, 1987.

Gueydan, F., Précigout, J., and Montesi, L. G.: Strain weakening enables continental plate tectonics, Tectonophysics, 631, 189-196, 2014.

© Author(s) 2017. CC-BY 3.0 License.

Hansen, L. N., Zimmerman, M. E., and Kohlstedt, D. L.: Grain boundary sliding in San Carlos olivine: Flow law parameters and crystallographic-preferred orientation, J. Geophys. Res-sol. Ea., 116(B8), 2011.

Hansen, L. N., Cheadle, M. J., John, B. E., Swapp, S. M., Dick, H. J., Tucholke, B. E., and Tivey, M. A.: Mylonitic deformation at the Kane oceanic core complex: Implications for the rheological behavior of oceanic detachment faults, Geochem. Geophys. Geosyst., 14(8), 3085-3108, 2013.

Helmstaedt, H., Anderson, O. L., and Gavasci, A. T.: Petrofabric studies of eclogite, spinel-Websterite, and spinel-lherzolite Xenoliths from kimberlite-bearing breccia pipes in southeastern Utah and northeastern Arizona, J. Geophys. Res., 77(23), 4350-4365, 1972.

Hidas, K., Falus, G., Szabó, C., Szabó, P. J., Kovács, I., and Földes, T.: Geodynamic implications of flattened tabular equigranular textured peridotites from the Bakony-Balaton Highland Volcanic Field (Western Hungary), J. Geodyn., 43(4), 484-503, 2007.

Hirth, G., and Kohlstedt, D. L.: Experimental constraints on the dynamics of the partially molten upper mantle: Deformation in the diffusion creep regime, J. Geophys. Res-sol. Ea., 100(B2), 1981-2001, 1995.

Hirth, G., and Kohlstedt, D.: Rheology of the upper mantle and the mantle wedge: A view from the experimentalists. Inside the subduction Factory, J. Eiler, American Geophysical Union, Washington, D.C., 83-105, 2003.

Holland, T. and Powell, R.: An internally consistent thermodynamic data set for phases of petrological interest, J. Metamorph. Geol., 16(3), 309-343, 1998.

Holtzman, B. K., Kohlstedt, D. L., Zimmerman, M. E., Heidelbach, F., Hiraga, T., and Hustoft, J.: Melt segregation and strain partitioning: implications for seismic anisotropy and mantle flow, Science, 301(5637), 1227-1230, 2003.

Jackson, J.: Strength of the continental lithosphere: time to abandon the jelly sandwich?, GSA today, 12(9), 4-9, 2002.

Ji, S., and Mainprice, D.: Recrystallization and fabric development in plagioclase, J. Geol., 98(1), 65-79, 1990.

Ji, S., Mainprice D., and Boudier, F.: Sense of shear in high-temperature movement zones from the fabric asymmetry of plagioclase feldspars, J. Struct. Geol., 10(1), 73-81, 1988.

Ji, S., Wirth, R., Rybacki, E., and Jiang, Z.: High-temperature plastic deformation of quartz-plagioclase multilayers by layer-normal compression, J. Geophys. Res., 105(B7), 16651, 2000.

Jiang, Z., Prior, D. J., and Wheeler, J.: Albite crystallographic preferred orientation and grain misorientation distribution in a low-grade mylonite: implications for granular flow, J. Struct. Geol., 22(11), 1663-1674, 2000.

Johnson, E. A. and Rossman, G. R.: The concentration and speciation of hydrogen in feldspars using FTIR and 1H MAS NMR spectroscopy, Am. Mineral., 88(5-6), 901-911, 2003.

Jung, H. and Karato, S.: Water-induced fabric transitions in olivine, Science, 293(5534), 1460-1463, doi: 10.1126/science.1062235, 2001.

Jung, H., Park, M., Jung, S., and Lee, J.: Lattice preferred orientation, water content, and seismic anisotropy of orthopyroxene, J. Earth Sci., 21(5), 555-568, 2010.

Kenkmann, T., and Dresen, G.: Dislocation microstructure and phase distribution in a lower crustal shear zone-an example from the Ivrea-Zone, Italy, Int. J. Earth Sci., 91(3), 445-458, 2002.

Kirby, S. H. and Christie, J. M.: Mechanical twinning in diopside Ca(Mg,Fe)Si2O6: structural mechanism and associated crystal defects, Phys. Chem. Miner., 1(2), 137-163, 1977.

Kirby, S. H. and Kronenberg, A. K.: Deformation of clinopyroxenite: Evidence for a transition in flow mechanisms and semibrittle behavior, J. Geophys. Res-Sol. Ea., 89(B5), 3177-3192, 1984.

Kohlstedt, D. L., Evans, B., and Mackwell, S. J.: Strength of the lithosphere: Constraints imposed by laboratory experiments, J. Geophys. Res-Sol. Ea., 100(B9), 17587-17602, 1995.

Kruse, R., Stünitz, H., and Kunze, K.: Dynamic recrystallization processes in plagioclase porphyroclasts, J. Struct. Geol., 23(11), 1781-1802, 2001.

© Author(s) 2017. CC-BY 3.0 License.

Langenheim, V. and Jachens, R.: Crustal structure of the Peninsular Ranges batholith from magnetic data: Implications for Gulf of California rifting, Geophys. Res. Lett., 30(11), 2003.

Legg, M. R.: Developments in understanding the tectonic evolution of the California Continental Borderland, 1991.

Lewis, J. L., Day, S. M., Magistrale, H., Castro, R. R., Rebollar, C., Astiz, L., Eakins, J., Vernon, F. L., and Brune, J. N.: Crustal thickness of the peninsular ranges and gulf extensional province in the Californias, J. Geophys. Res., 106(B7), 13,599-13,611, 2001.

Lockner, D. A., Morrow, C., Moore, D., and Hickman, S.: Low strength of deep San Andreas fault gouge from SAFOD core, Nature, 472(7341), 82-85, 2011.

Long, M. D.: Frequency-dependent shear wave splitting and heterogeneous anisotropic structure beneath the Gulf of California region, Phys. Earth Planet. Inter., 182(1), 59-72, 2010.

Lopez-Sanchez, M. A. and Llana-Fúnez, S.: An evaluation of different measures of dynamically recrystallized grain size for paleopiezometry or paleowattometry studies, Solid Earth, 6(2), 475, 2015.

Luhr, J. F., and Aranda-Gómez, J. J.: Mexican peridotite xenoliths and tectonic terranes: correlations among vent location, texture, temperature, pressure, and oxygen fugacity, J. Petrol., 38(8), 1075-1112, 1997.

Luhr, J. F., Aranda-Gómez, J. J., and Housh, T. B.: San Quintín volcanic field, Baja California Norte, México: geology, petrology, and geochemistry, J. Geophys. Res-Sol. Ea., 100(B6), 10353-10380, 1995.

Mehl, L., and Hirth, G.: Plagioclase preferred orientation in layered mylonites: Evaluation of flow laws for the lower crust, J. Geophys. Res-Sol. Ea., 113(B5), 2008.

Miranda, E. A., Hirth, G., and John, B. E.: Microstructural evidence for the transition from dislocation creep to dislocation-accommodated grain boundary sliding in naturally deformed plagioclase, J. Struct. Geol., 92, 30-45, 2016.

Mosenfelder, J. L., Rossman, G. R., and Johnson E. A.: Hydrous species in feldspars: A reassessment based on FTIR and SIMS, Am. Mineral., 100(5-6), 1209-1221, 2015.

Nicolas, A. and Poirier,J. P.: Crystalline Plasticity and Solid State Flow in Metamorphic Rocks, John Wiley & Sons, 1976.

Olsen, T. S., and Kohlstedt, D. L.: Analysis of dislocations in some naturally deformed plagioclase feldspars, Phys. Chem. Miner., 11(4), 153-160, 1984.

Palasse, L., Vissers, R., Paulssen, H., Basu, A., and Drury, M.: Microstructural and seismic properties of the upper mantle underneath a rifted continental terrane (Baja California): An example of sub-crustal mechanical asthenosphere?, Earth Planet. Sci. Lett., 345, 60-71, 2012.

Paulssen, H. and de Vos, D.: Slab remnants beneath the Baja California peninsula: Seismic constraints and tectonic implications, Tectonophysics, 2016.

Peslier, A. H., and Luhr, J. F.: Hydrogen loss from olivines in mantle xenoliths from Simcoe (USA) and Mexico: Mafic alkalic magma ascent rates and water budget of the sub-continental lithosphere, Earth Planet. Sci. Lett., 242(3), 302-319, 2006.

Piazolo, S., Bons, P. D., Jessell, M. W., Evans, L., and Passchier, C. W.: Dominance of Microstructural Processes and Their Effect on Microstructural Development: Insights from Numerical Modelling of Dynamic Recrystallization, Geol. Soc. London, Sp. Publ., 200, 149-170, 2002.

Plattner, C., Malservisi, R., Dixon, T. H., LaFemina, P., Sella, G., Fletcher, J., and Suarez-Vidal, F.: New constraints on relative motion between the Pacific plate and Baja California microplate (Mexico) from GPS measurements, Geophys. J. Int., 170(3), 1373-1380, 2007.

Plattner, C., Malservisi, R., and Govers, R.: On the plate boundary forces that drive and resist Baja California motion, Geology, 37(4), 359-362, 2009.

Pollitz, F. F., Wicks, C., and Thatcher, W.: Mantle flow beneath a continental strike-slip fault: postseismic deformation after the 1999 Hector Mine earthquake, Science, 293(5536), 1814-1818, doi: 10.1126/science.1061361 [doi], 2001.

© Author(s) 2017. CC-BY 3.0 License.

Précigout, J., and Hirth, G.: B-type olivine fabric induced by grain boundary sliding, Earth Planet. Sci. Lett., 395, 231-240, 2014.

Ree, J.H.: Grain boundary sliding and development of grain boundary openings in experimentally deformed octachloropropane, J. Struct. Geol., 16, 403–418, 1994.

Reyners, M., Eberhart-Phillips, D., and Stuart, G.: The role of fluids in lower-crustal earthquakes near continental rifts, Nature, 446(1075-1078), doi:10.1038/nature05743, 2007

Rogers, G., Saunders A., Terrell D., Verma S., and Marriner G.: Geochemistry of Holocene volcanic rocks associated with ridge subduction in Baja California, Mexico, Nature, 315(6018), 389-392, 1985.

Rothstein, D. A. and Manning, C. E.: Geothermal gradients in continental magmatic arcs: Constraints from the eastern Peninsular Ranges batholith, Baja California, México, Spec. Pap.-Geol. Soc. Am., 337-354, 2003.

Rudnick, R. L.: Xenoliths—samples of the lower continental crust, Continental lower crust, 23, 269-316, 1992.

Rybacki, E., and Dresen, G.: Dislocation and diffusion creep of synthetic anorthite aggregates, J. Geophys. Res-Sol. Ea., 105(B11), 26017-26036, 2000.

Rybacki, E. M., Gottschalk, R. W., and Dresen, G.: Influence of water fugacity and activation volume on flow properties of fine-grained anorthite aggregates, J. Geophys. Res., 111, B03203, 2006.

Satsukawa, T., Ildefonse, B., Mainprice, D., Morales, L., Michibayashi, K., and Barou, F.: A database of plagioclase crystal preferred orientations (CPO) and microstructures-implications for CPO origin, strength, symmetry and seismic anisotropy in gabbroic rocks, Solid Earth, 4(2), 511, 2013.

Schmidt, K., Wetmore, P., Alsleben, H., and Paterson, S.: Mesozoic tectonic evolution of the southern Peninsular Ranges batholith, Baja California, Mexico: Long-lived history of a collisional segment in the Mesozoic Cordilleran arc, Geol. Soc. Am. Mem., 211, 645-668, 2014.

Silver, L. and Chappell, B.: The Peninsular Ranges Batholith: an insight into the evolution of the Cordilleran batholiths of southwestern North America, Transactions of the Royal Society of Edinburgh: Earth Sci., 79(2-3), 105-121, 1988.

Skemer, P., and Karato, S. I.: Sheared lherzolite xenoliths revisited, J. Geophys. Res-Sol. Ea., 113(B7), 2008.

Soustelle, V., Tommasi, A., Demouchy, S., and Ionov, D.: Deformation and fluid–rock interaction in the supra-subduction mantle: microstructures and water contents in peridotite xenoliths from the Avacha Volcano, Kamchatka, J. Petrol., 51(1-2), 363-394, 2010.

Spencer, J. E. and Normark, W. R.: Tosco-Abreojos fault zone: A Neogene transform plate boundary within the Pacific margin of southern Baja California, Mexico, Geology, 7(11), 554-557, 1979.

Stock, J. and Hodges, K.: Pre-Pliocene extension around the Gulf of California and the transfer of Baja California to the Pacific Plate, Tectonics, 8(1), 99-115, 1989.

Storey, M., Rogers, G., Saunders, A., and Terrell, D.: San Quintín volcanic field, Baja California, Mexico:'within-plate'magmatism following ridge subduction, Terra Nova, 1(2), 195-202, 1989.

Stünitz, H., Gerald, J. F., and Tullis, J.: Dislocation generation, slip systems, and dynamic recrystallization in experimentally deformed plagioclase single crystals, Tectonophysics, 372(3), 215-233, 2003.

Svahnberg, H., and Piazolo, S.: The initiation of strain localisation in plagioclase-rich rocks: Insights from detailed microstructural analyses, J. Struct. Geol., 32(10), 1404-1416, 2010.

Taylor, W.: An experimental test of some geothermometer and geobarometer formulations for upper mantle peridotites with application to the thermobarometry of fertile lherzolite and garnet websterite, Neues Jb. Miner.-Abh., 381-408, 1998.

Teyssier, C., and Tikoff, B.: Strike-slip partitioned transpression of the San Andreas fault system: a lithospheric-scale approach, Geol. Soc. Spec. Publ., 135(1), 143-158, 1998.

Thatcher, W., and Pollitz, F. F.: Temporal evolution of continental lithospheric strength in actively deforming regions, Gsa Today, 18(4/5), 4, 2008.

© Author(s) 2017. CC-BY 3.0 License.

Thorkelson, D. J., and Breitsprecher, K.: Partial melting of slab window margins: genesis of adakitic and non-adakitic magmas, Lithos, 79(1), 25-41, 2005.

Titus, S. J., Medaris, L. G., Wang, H. F., and Tikoff, B.: Continuation of the San Andreas fault system into the upper mantle: evidence from spinel peridotite xenoliths in the Coyote Lake basalt, central California, Tectonophysics, 429(1), 1-20, 2007.

Todd, V. R., Shaw, S. E., and Hammarstrom, J. M.: Cretaceous plutons of the Peninsular Ranges batholith, San Diego and westernmost Imperial counties, California: Intrusion across a Late Jurassic continental margin, Spec. Pap.-Geol Soc. Am., 185-236, 2003.

Tommasi, A., Tikoff, B., and Vauchez, A.: Upper mantle tectonics: three-dimensional deformation, olivine crystallographic fabrics and seismic properties, Earth Planet. Sci. Lett., 168(1), 173-186, 1999.

Tommasi, A., Godard, M., Coromina, G., Dautria, J. M., and Barsczus, H.: Seismic anisotropy and compositionally induced velocity anomalies in the lithosphere above mantle plumes: a petrological and microstructural study of mantle xenoliths from French Polynesia, Earth Planet. Sci. Lett., 227(3), 539-556, 2004.

Toriumi, M.: Relation between dislocation density and subgrain size of naturally deformed olivine in peridotites, Contrib. Mineral. Petr., 68(2), 181-186, 1979.

Trepmann, C. A., and Stöckhert, B.: Quartz microstructures developed during non-steady state plastic flow at rapidly decaying stress and strain rate, J. Struct. Geol., 25(12), 2035-2051, 2003.

Twiss, R. J.: Theory and applicability of a recrystallized grain size paleopiezometer, in Stress in the Earth Anonymous , Springer, pp. 227-244, 1977.

Ulrich, S. and Mainprice, D.: Does cation ordering in omphacite influence development of lattice-preferred orientation?, J. Struct. Geol., 27(3), 419-431, 2005.

Umhoefer, P. J.: Why did the Southern Gulf of California rupture so rapidly?—Oblique divergence across hot, weak lithosphere along a tectonically active margin, GSA Today, 21(11), 4-10, 2011.

Umhoefer, P. J. and Dorsey, R. J.: Translation of terranes: lessons from central Baja California, Mexico, Geology, 25(11), 1007-1010, 1997.

Underwood, E.: Quantitative Stereology, Addison-Wesley, Reading, Mass, 1970.

Valcke, S., Pennock, G., Drury, M., and De Bresser, J.: Electron backscattered diffraction as a tool to quantify subgrains in deformed calcite, J. Microsc., 224(3), 264-276, 2006.

Van der Wal, D., Chopra, P., Drury, M., and Gerald, J. F.: Relationships between dynamically recrystallized grain size and deformation conditions in experimentally deformed olivine rocks, Geophys. Res. Lett., 20(14), 1479-1482, 1993.

Vauchez, A., Dineur, F., and Rudnick, R.: Microstructure, texture and seismic anisotropy of the lithospheric mantle above a mantle plume: insights from the Labait volcano xenoliths (Tanzania), Earth Planet. Sci. Lett., 232(3), 295-314, 2005.

Warren, J. M., and Hirth, G.: Grain size sensitive deformation mechanisms in naturally deformed peridotites, Earth Planet. Sci. Lett., 248(1), 438-450, 2006.

Wilks, K. R., and Carter, N. L.: Rheology of some continental lower crustal rocks, Tectonophysics, 182(1-2), 57-77, 1990.

Xie, Y., Wenk, H., and Matthies, S.: Plagioclase preferred orientation by TOF neutron diffraction and SEM-EBSD, Tectonophysics, 370(1), 269-286, 2003.

Zhang, X., Paulssen, H., Lebedev, S., and Meier, T.: 3D shear velocity structure beneath the Gulf of California from Rayleigh wave dispersion, Earth Planet. Sci. Lett., 279(3), 255-262, 2009.

Zhang, X., and Paulssen, H.: Geodynamics of the Gulf of California from surface wave tomography, Phys. Earth Planet. Inter., 192-193, 59–67, 2012.

Solid Earth Discuss., doi:10.5194/se-2017-45, 2017
Manuscript under review for journal Solid Earth
Discussion started: 11 May 2017
© Author(s) 2017. CC-BY 3.0 License.

Figure Captions

Figure 1: Geological map of Baja California, Mexico, showing the location of the San Quintin volcanic field (SQ) (modified after Langenheim and Jachens, 2003). The San Benito (SB) and Tosco Abreojos (TAF) faults comprise parts of the Baja California Shear Zone. Arrows indicate the relative movement of the Pacific plate and the Baja California microplate with that of the North American plate (Plattner et al., 2007). Inset is a tectonic map of the Pacific-North American plate boundary, showing the location of the Baja California Shear Zone and the San Quintin volcanic field relative to the San Andreas Fault (SAF) and the Coyote Lake volcanic field (CL). EPR: East Pacific Rise.

Figure 2: Typical microstructures in the San Quintin gabbroic and mafic granulite xenoliths. All photomicrographs are under crossed-polarized light. (a) Cumulate microstructure of the gabbroic xenolith SQL-13A characterized by crystallized pyroxenes and interstitial plagioclase. (b) Core-and-mantle microstructure of clinopyroxene in granulite xenolith SQW-75. The elongated cluster of clinopyroxene and orthopyroxene defines the foliation (upper right to lower left) in the granulite. (c) Granoblastic microstructure with interlobate boundaries between plagioclase grains in xenolith SQW-110. (d) Melt patch between pyroxene and plagioclase aggregates in SQ-16. (e) Granoblastic microstructure in granulite SQW-75. Large plagioclase grains with straight grain boundaries (small white triangles) meeting at 120° triple junctions and a quadruple junctions (larger white triangle in the center). (f) Equigranular mosaic microstructure in lherzolite xenolith SQ-68. Quadruple junction (large white triangle in the center) associated with straight and aligned grain boundaries (described by the small white triangles) of olivine grains.

Figure 3: Examples of EBSD maps. All maps have upper edge parallel to the observed lineation, with the foliation being normal to the map. (a) EBSD phase map layered on a band contrast map in granulite SQ-16. (b-d) EBSD maps of Euler orientation layered on band contrast maps. The white box in (a) shows the location of (b). (c) is from xenolith SQW-75 and (d) from SQW-115. Black arrows show subgrain boundaries in plagioclase. White arrows point to quadruple junctions. White triangles delineate aligned grain boundaries.

Figure 4: SEM-BSE images showing typical microstructures in the San Quintin xenoliths. (a) Symplectite with intergrown orthopyroxene, spinel, plagioclase and olivine in SQW-75. (b) Melt patch containing plagioclase, olivine, clinopyroxene and orthopyroxene. Compositional variation between two types of plagioclase can be seen in the lower left part of the image (SQW-114). (c), Orthopyroxene with a rim containing olivine, plagioclase and clinopyroxene (SQW-115). (d) Inclusion in a clinopyroxene porphyroclast. The inclusion contains spinel with a magnetite rim, orthopyroxene, plagioclase and olivine (SQW-75).

Figure 5: Histogram showing the anorthite content of recrystallized plagioclase grains and plagioclase grains in symplectites.

Figure 6: Constructed P-T pseudosections for samples SQ-16, SQW 75, and SQW-114. Molar composition is indicated in the text boxes. The observed mineral assemblage is indicated by a red outline. (a) SQ-16 pseudosection, the dashed lines illustrate the range of Al2O3 in clinopyroxene. (b) SQW-75 pseudosection, the dashed lines illustrate the range of the magnesium number found in clinopyroxene and orthopyroxene (not shown in the figure). (c) SQW-114 pseudosection, the dashed line shows the range of the magnesium numbers of orthopyroxene and the dashed line with dots shows the range of Al_2O_3 in orthopyroxene.

Figure 7: Representative IR spectra for plagioclase in the xenolith samples, with measured absorbances normalized to 1 mm sample thickness. (a) SQW-76. (b) SQW-78. (c) SQW-115.

Figure 8: Crystallographic orientations and low-angle misorientations of (a) plagioclase, (b) clinopyroxene, (c) orthopyroxene, and (d) olivine grains. Crystallographic orientations are plotted as one point per grain data sets in lower hemisphere equal area projections, relative to the observed foliation and lineation. Color scales are for multiples of uniform distribution. For each sample, the J-index, as well as the number of grains analyzed, are given. Misorientation axes are from correlated misorientation angles between 2° and 10°. Inverse pole figures are in the crystallographic reference frame.

© Author(s) 2017. CC-BY 3.0 License.

Figure 9: EBSD map and crystallographic orientations illustrating the control of the local flow field on plagioclase and clinopyroxene CPO. (a) Same EBSD map with Fig. 3a showing the location of the domains in which plagioclase and clinopyroxene domainal CPOs were analyzed. (b, c) Domainal plagioclase and clinopyroxene CPOs. Crystallographic orientations are plotted as one point per grain data sets in lower hemisphere equal area projections, relative to the observed foliation and lineation. Color scales are for multiples of uniform distribution. For each sample, the J-index and the number of grains analyzed are given. White dashed lines show the local foliation. In P2 and C2 the shear planes are subparallel to the fault trace.

Figure 10: Estimated temperatures and pressures for the San Quitnin xenoliths. The conditions for the lower crustal xenoliths are from this study. The conditions for the upper mantle xenoliths are from (1) Luhr and Aranda-Gómez (1997) and (2) Cabanes and Mercier (1988). Crustal geotherms are from (3) Rothstein and Manning (2003) and (4) Negrete-Aranda et al. (2013). Mantle geotherms are from (1) Luhr and Aranda-Gómez (1997) for surface heat flows of 120 and 150 mW/m^2. The red dash line described the inferred geotherm which describes the P-T conditions in the San Quintin lower crustal and upper mantle xenoliths.

Figure 11: (a) Shear stress, (b) Strain rate, and (c) Viscosity as a function of depth for the San Quintin xenoliths. Error bars reflect the estimated uncertainties in pressure (vertical) and temperature (horizontal) conditions of deformation propagated to determine corresponding errors in stress, strain rate, and viscosity. The red dash line in (c) shows the viscosity structure of the lower crust based on the inferred near isothermal conditions. The Moho depth is from Paulssen and De Vos (2016).

Solid Earth Discuss., doi:10.5194/se-2017-45, 2017
Manuscript under review for journal Solid Earth
Discussion started: 11 May 2017
© Author(s) 2017. CC-BY 3.0 License.

1055 **Table 1.** Equilibration temperature and pressure, grain size, and differential stress

		Phase Equilibria					
Xenolith	Mean 2-Px T (°C)	T (°C)	P (MPa)	D_{plg} (μm)	σ_{plg} (MPa)	D_{ol} (μm)	σ_{ol} (MPa)
SQ-16	751 ± 27	630−700	300−370	122	33	340	17
SQL-48	765 ± 36	–	–	346	–	–	–
SQW-75	759 ± 25	680−860	400−530	454	13	–	–
SQW-76	–	–	–	482	–	–	–
SQW-110	886 ± 87	–	–	528	12	–	–
SQW-114	886 ± 32	700−980	450−580	–	–	–	–
SQW-115	854 ± 28	–	–	413	–	–	–
SQ-68	–	–	–	–	–	361	17

2-Px T, average equilibration temperature from two-pyroxene geothermometry; T, equilibration temperature from phase equilibria modeling; P, equilibration pressure from phase equilibria modeling; D, equivalent circular diameter grain size; σ, differential stress.

Solid Earth Discuss., doi:10.5194/se-2017-45, 2017
Manuscript under review for journal Solid Earth
Discussion started: 11 May 2017
© Author(s) 2017. CC-BY 3.0 License.

1060

Table 2. H_2O concentrations in plagioclase

Xenolith	IR band area (cm^{-2})	Total band area (cm^{-2})	ppm H_2O wt%	wt%
SQW-78	180−480	237−4974	15−317	0.0015−0.032
SQW-115	80−420	105−352	7−278	0.0007−0.029
SQW-76	1810−6320	2382−65492	151−4178	0.015−0.42

Solid Earth Discuss., doi:10.5194/se-2017-45, 2017
Manuscript under review for journal Solid Earth
Discussion started: 11 May 2017
© Author(s) 2017. CC-BY 3.0 License.

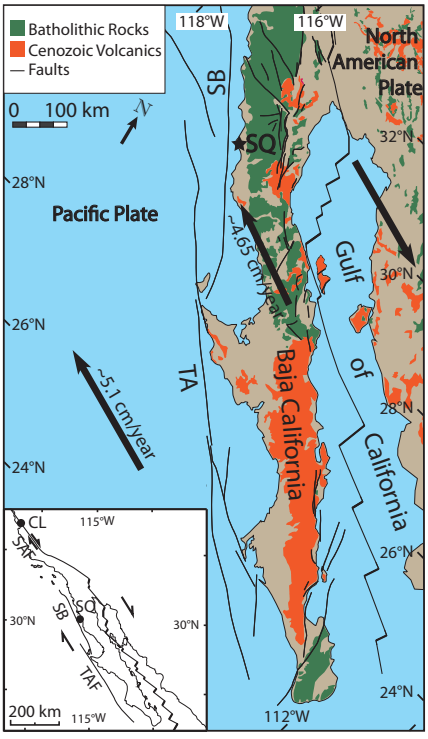

Figure 1: Geological map of Baja California, Mexico, showing the location of the San Quintin volcanic field (SQ) (modified after Langenheim and Jachens, 2003). The San Benito (SB) and Tosco Abreojos (TA) faults comprise parts of the Baja California Shear Zone. Arrows indicate the relative movement of the Pacific plate and the Baja California microplate with that of the North American plate (Plattner et al., 2007). Inset is a tectonic map of the Pacific-North American plate boundary, showing the location of the Baja California Shear Zone and the San Quintin volcanic field relative to the San Andreas Fault (SAF) and the Coyote Lake volcanic field (CL).

Solid Earth Discuss., doi:10.5194/se-2017-45, 2017
Manuscript under review for journal Solid Earth
Discussion started: 11 May 2017
© Author(s) 2017. CC-BY 3.0 License.

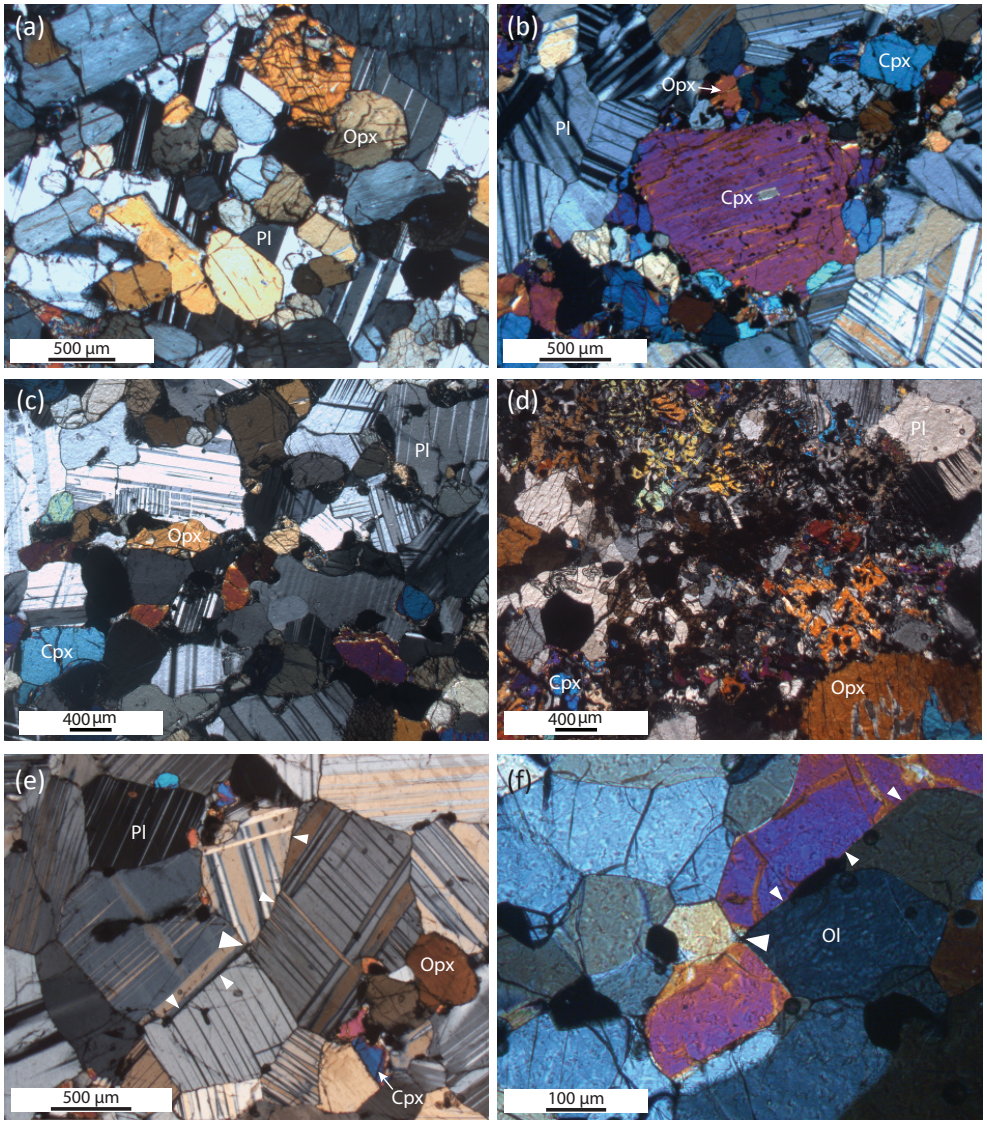

Figure 2: Typical microstructures in the San Quintin gabbroic and mafic granulite xenoliths. All photomicrographs are under crossed-polarized light. (a) Cumulate microstructure of the gabbroic xenolith SQL-13A characterized by crystallized pyroxenes and interstitial plagioclase. (b) Core-and-mantle microstructure of clinopyroxene in granulite xenolith SQW-75. The elongated cluster of clinopyroxene and orthopyroxene defines the foliation (upper right to lower left) in the granulite. (c) Granoblastic microstructure with interlobate boundaries between plagioclase grains in xenolith SQW-110. (d) Melt patch between pyroxene and plagioclase aggregates in SQ-16. (e) Granoblastic microstructure in granulite SQW-75. Large plagioclase grains with straight grain boundaries (small white triangles) meeting at 120° triple junctions and a quadruple junctions (larger white triangle in the center). (f) Equigranular mosaic microstructure in lherzolite xenolith SQ-68. Quadruple junction (large white triangle in the center) associated with straight and aligned grain boundaries (described by the small white triangles) of olivine grains.

Solid Earth Discuss., doi:10.5194/se-2017-45, 2017
Manuscript under review for journal Solid Earth
Discussion started: 11 May 2017
© Author(s) 2017. CC-BY 3.0 License.

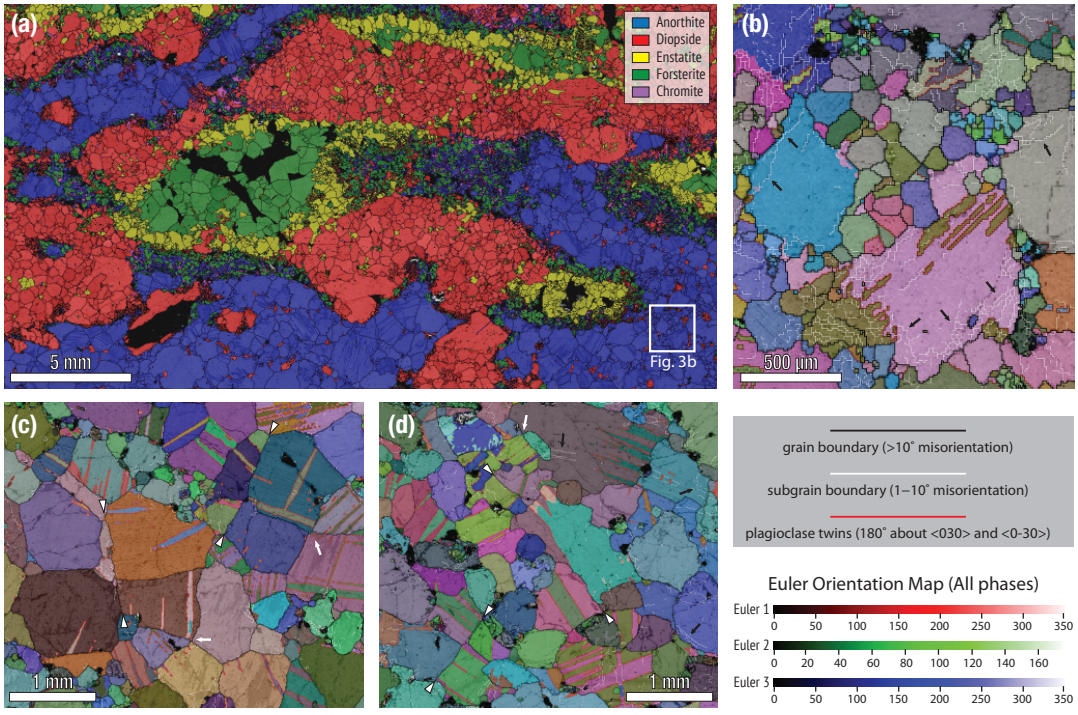

Figure 3: Examples of EBSD maps. All maps have upper edge parallel to the observed lineation, with the foliation being normal to the map. (a) EBSD phase map layered on a band contrast map in granulite SQ-16. (b-d) EBSD maps of Euler orientation layered on band contrast maps. The white box in (a) shows the location of (b). (c) is from xenolith SQW-75 and (d) from SQW-115. Black arrows show subgrain boundaries in plagioclase. White arrows point to quadruple junctions. White triangles delineate aligned grain boundaries.

Solid Earth Discuss., doi:10.5194/se-2017-45, 2017
Manuscript under review for journal Solid Earth
Discussion started: 11 May 2017
© Author(s) 2017. CC-BY 3.0 License.

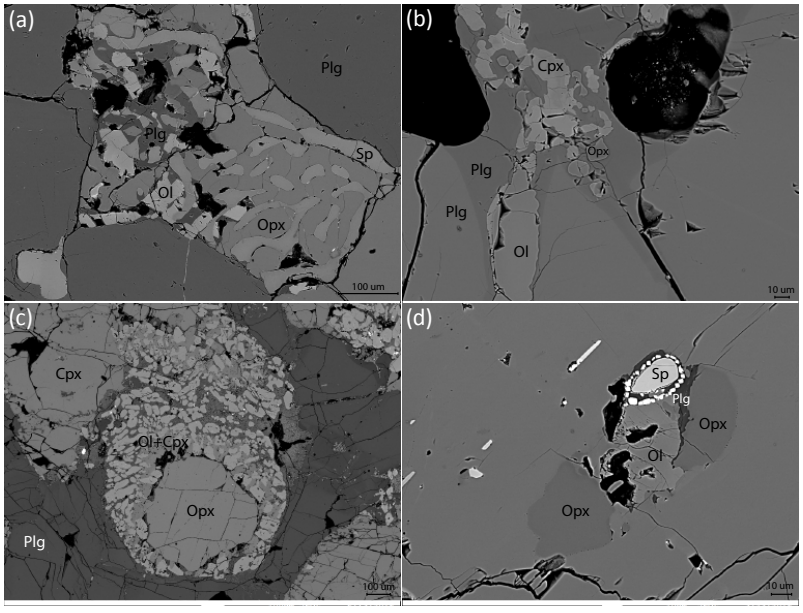

Figure 4: SEM-BSE images showing typical microstructures in the San Quintin xenoliths. (a) Symplectite with intergrown orthopyroxene, spinel, plagioclase and olivine in SQW-75. (b) Melt patch containing plagioclase, olivine, clinopyroxene and orthopyroxene. Compositional variation between two types of plagioclase can be seen in the lower left part of the image (SQW-114). (c) Orthopyroxene with a rim containing olivine, plagioclase and clinopyroxene (SQW-115). (d) Inclusion in a clinopyroxene porphyroclast. The inclusion contains spinel with a magnetite rim, orthopyroxene, plagioclase and olivine (SQW-75).

Solid Earth Discuss., doi:10.5194/se-2017-45, 2017
Manuscript under review for journal Solid Earth
Discussion started: 11 May 2017
© Author(s) 2017. CC-BY 3.0 License.

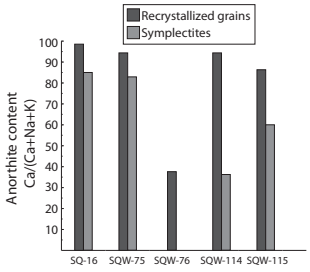

Figure 5: Histogram showing the anorthite content of recrystallized plagioclase grains and plagioclase grains in symplectites.

Solid Earth Discuss., doi:10.5194/se-2017-45, 2017
Manuscript under review for journal Solid Earth
Discussion started: 11 May 2017
© Author(s) 2017. CC-BY 3.0 License.

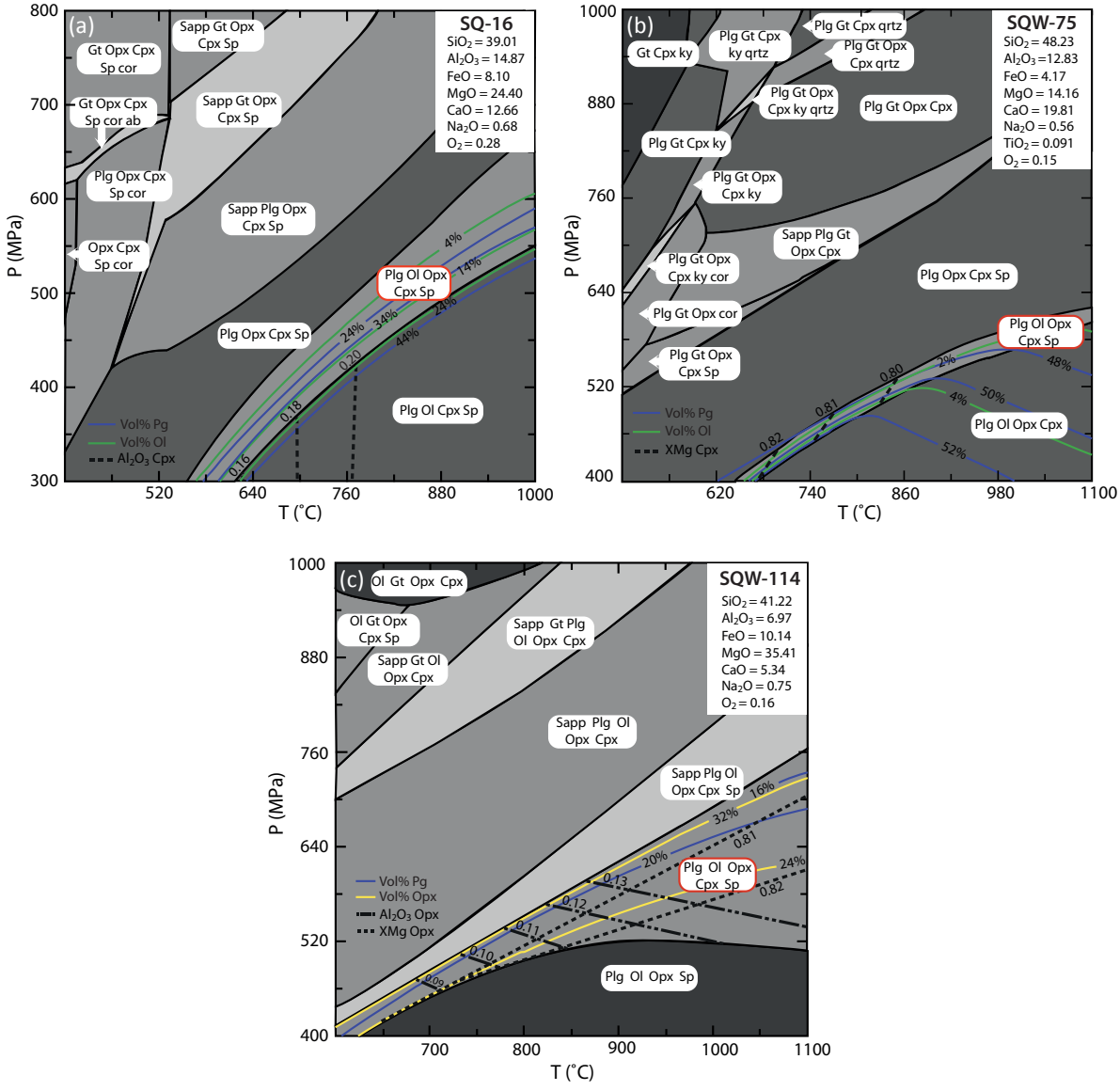

Figure 6: Constructed P-T pseudosections for samples SQ-16, SQW 75, and SQW-114. Molar composition is indicated in the text boxes. The observed mineral assemblage is indicated by a red outline. (a) SQ-16 pseudosection, the dashed lines illustrate the range of Al_2O_3 in clinopyroxene. (b) SQW-75 pseudosection, the dashed lines illustrate the range of the magnesium number found in clinopyroxene and orthopyroxene (not shown in the figure). (c) SQW-114 pseudosection, the dashed line shows the range of the magnesium numbers of orthopyroxene and the dashed line with dots shows the range of Al_2O_3 in orthopyroxene.

Solid Earth Discuss., doi:10.5194/se-2017-45, 2017
Manuscript under review for journal Solid Earth
Discussion started: 11 May 2017
© Author(s) 2017. CC-BY 3.0 License.

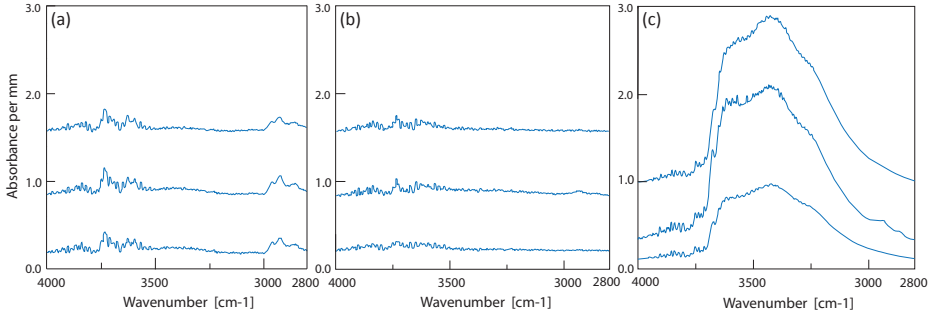

Figure 7: Representative IR spectra for plagioclase in the xenolith samples, with measured absorbances normalized to 1 mm sample thickness. (a) SQW-76. (b) SQW-78. (c) SQW-115.

Solid Earth Discuss., doi:10.5194/se-2017-45, 2017
Manuscript under review for journal Solid Earth
Discussion started: 11 May 2017
© Author(s) 2017. CC-BY 3.0 License.

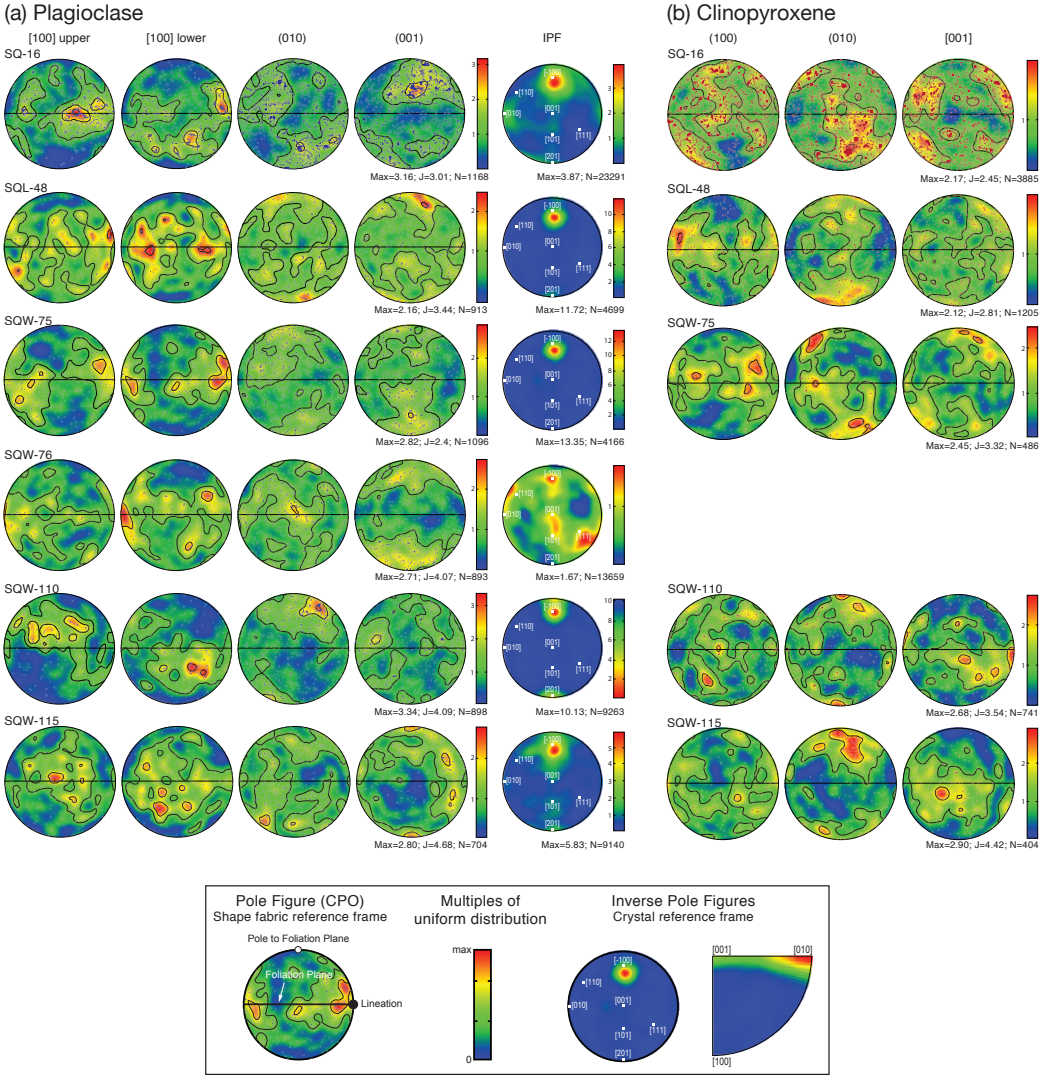

Figure 8: Crystallographic orientations and low-angle misorientations of (a) plagioclase, (b) clinopyroxene, (c) orthopyroxene, and (d) olivine grains. Crystallographic orientations are plotted as one point per grain data sets in lower hemisphere equal area projections, relative to the observed foliation and lineation. Color scales are for multiples of uniform distribution. For each sample, the J-index, as well as the number of grains analyzed, are given. Misorientation axes are from correlated misorientation angles between 2° and 10°. Inverse pole figures are in the crystallographic reference frame.

Solid Earth Discuss., doi:10.5194/se-2017-45, 2017
Manuscript under review for journal Solid Earth
Discussion started: 11 May 2017
© Author(s) 2017. CC-BY 3.0 License.

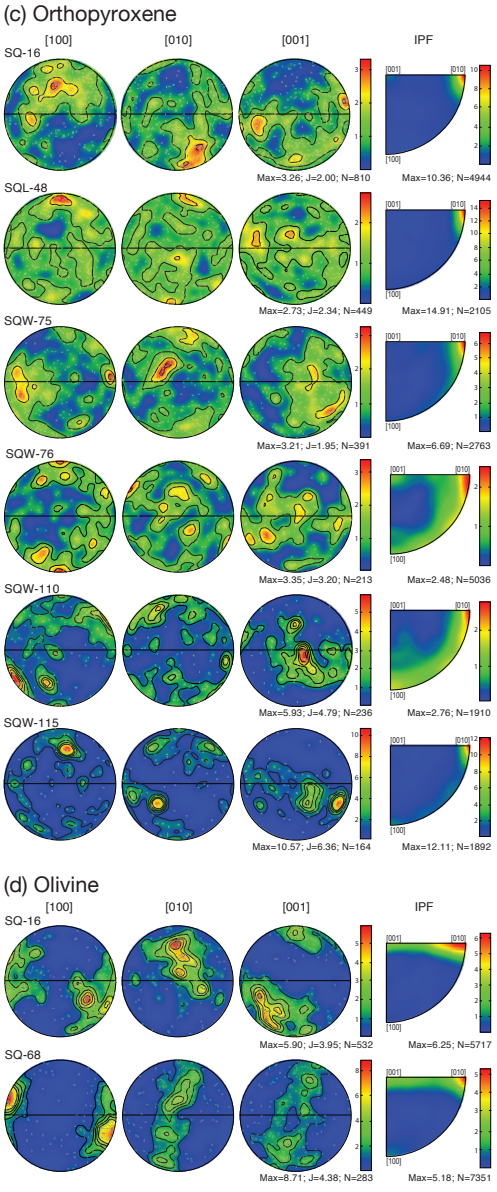

Figure 8: (continued)

Solid Earth Discuss., doi:10.5194/se-2017-45, 2017
Manuscript under review for journal Solid Earth
Discussion started: 11 May 2017
© Author(s) 2017. CC-BY 3.0 License.

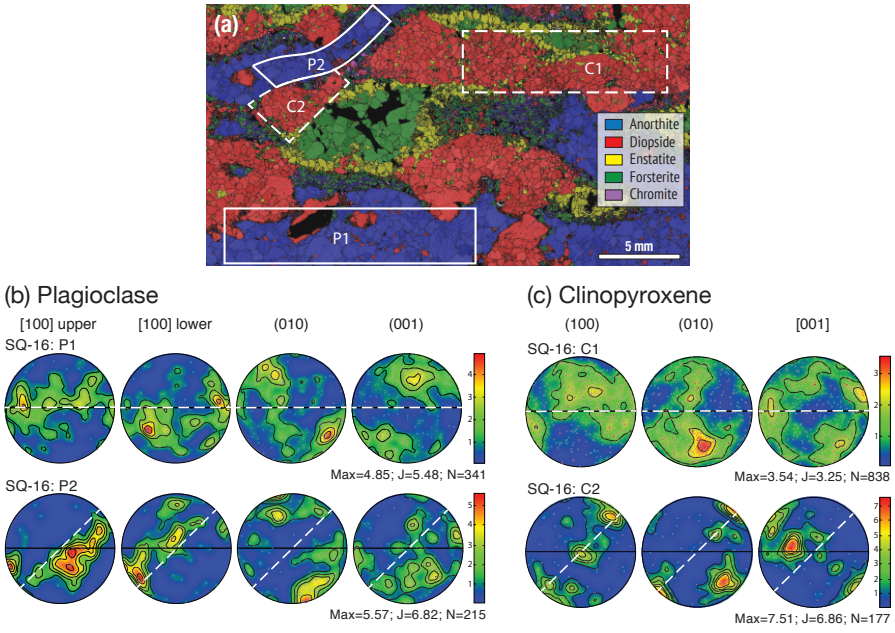

Figure 9: EBSD map and crystallographic orientations illustrating the control of the local flow field on plagioclase and clinopyroxene CPO. (a) Same EBSD map with Fig. 3a showing the location of the domains in which plagioclase and clinopyroxene domainal CPOs were analyzed. (b, c) Domainal plagioclase and clinopyroxene CPOs. Crystallographic orientations are plotted as one point per grain data sets in lower hemisphere equal area projections, relative to the observed foliation and lineation. Color scales are for multiples of uniform distribution. For each sample, the J-index and the number of grains analyzed are given. White dashed lines show the local foliation. In P2 and C2 the shear planes are subparallel to the fault trace.

Solid Earth Discuss., doi:10.5194/se-2017-45, 2017
Manuscript under review for journal Solid Earth
Discussion started: 11 May 2017
© Author(s) 2017. CC-BY 3.0 License.

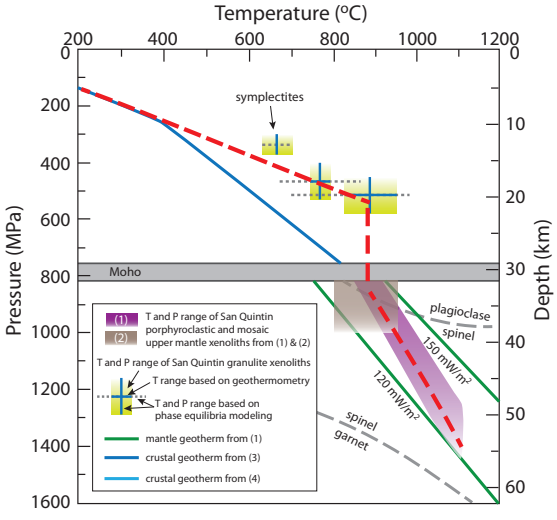

Figure 10: Estimated temperatures and pressures for the San Quitnin xenoliths. The conditions for the lower crustal xenoliths are from this study. The conditions for the upper mantle xenoliths are from (1) Luhr and Aranda-Gómez (1997) and (2) Cabanes and Mercier (1988). Crustal geotherms are from (3) Rothstein and Manning (2003) and (4) Negrete-Aranda et al. (2013). Mantle geotherms are from (1) Luhr and Aranda-Gómez (1997) for surface heat flows of 120 and 150 mW/m^2. The red dashed line described the inferred geotherm which describes the P-T conditions in the San Quintin lower crustal and upper mantle xenoliths.

Solid Earth Discuss., doi:10.5194/se-2017-45, 2017
Manuscript under review for journal Solid Earth
Discussion started: 11 May 2017
© Author(s) 2017. CC-BY 3.0 License.

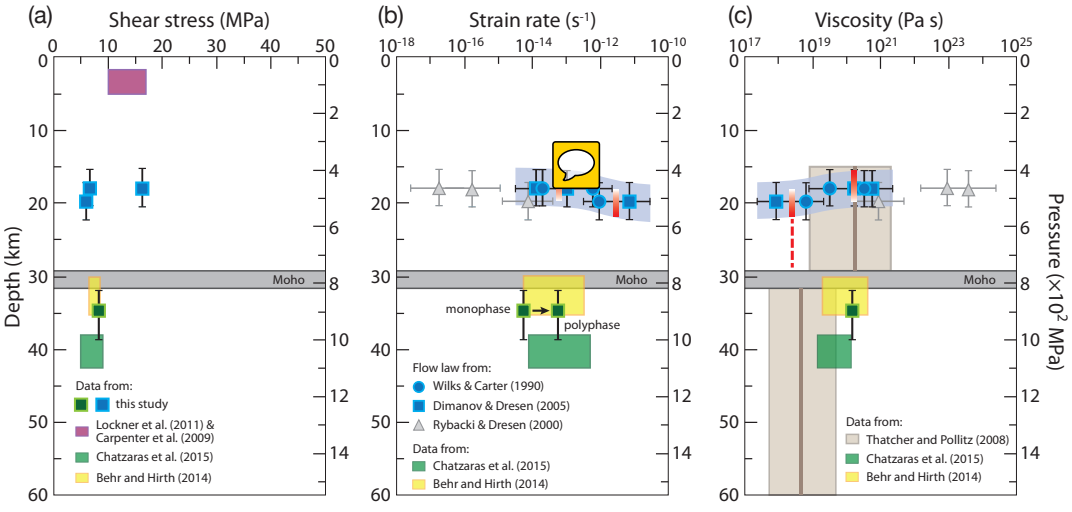

Figure 11: (a) Shear stress, (b) Strain rate, and (c) Viscosity as a function of depth for the San Quintin xenoliths. Error bars reflect the estimated uncertainties in pressure (vertical) and temperature (horizontal) conditions of deformation propagated to determine corresponding errors in stress, strain rate, and viscosity. The red dashed line in (c) shows the viscosity structure of the lower crust based on the inferred near isothermal conditions. The Moho depth is from Paulssen and De Vos (2016).